Oncogenic Kras induces Nix-mediated mitophagy to promote pancreatic cancer

Timothy J. Humpton[1,*], Brinda Alagesan[2,3,4,*], Gina M. DeNicola[5], Dan Lu[6], Georgi N. Yordanov[2,3], Carl S. Leonhardt[2,3], Melissa A. Yao[2,3], Priya Alagesan[2,3], Maya N. Zaatari[2,3], Youngkyu Park[2,3], Jeremy N. Skepper[7], Kay F. Macleod[8], Pedro A. Perez-Mancera[9], Michael P. Murphy[10], Gerard I. Evan[6], Karen H. Vousden[11], David A. Tuveson[2,3#]

1. Cancer Research UK Beatson Institute, Glasgow G61 1BD, United Kingdom
2. Cold Spring Harbor Laboratory, Cold Spring Harbor, NY 11724 USA
3. Lustgarten Foundation Pancreatic Cancer Research Laboratory, Cold Spring Harbor, NY 11724
4. Medical Scientist Training Program, Stony Brook University, Stony Brook, NY 11794
5. Department of Cancer Physiology, Moffitt Cancer Center and Research Institute, Tampa, FL, 33612 USA
6. Department of Biochemistry, University of Cambridge, Cambridge CB2 1QW, United Kingdom
7. Cambridge Advanced Imaging Centre, Department of Physiology, Development, and Neuroscience, University of Cambridge, CB2 3DY Cambridge, United Kingdom
8. The Ben May Department for Cancer Research, University of Chicago, Chicago, IL 60637 USA
9. Department of Molecular and Clinical Cancer Medicine, University of Liverpool, Liverpool, United Kingdom
10. MRC Mitochondrial Biology Unit, University of Cambridge, CB2 0XY Cambridge, United Kingdom
11. The Francis Crick Institute, London NW1 1AT, United Kingdom

*Contributed equally

[#]Corresponding author:
Cold Spring Harbor Laboratory
1 Bungtown Road
Cold Spring Harbor, NY 11724
Tel: 516-367-5246
Dtuveson@cshl.edu

Running title: Nix-mediated mitophagy promotes pancreatic cancer

Disclosure of potential conflict of interest: D.A. Tuveson serves on the Scientific Advisory Board of Leap Therapeutics, Surface Oncology, and Bethyl Laboratory, which is not related to the subject matter of this manuscript. K. Vousden is on the Board of Directors and shareholder of Bristol Myers Squib, on the Advisory Board and shareholder of Grail Inc., and on the advisory board of PMV Pharma and RAZE therapeutics.

Abstract

Activating *KRAS* mutations are found in nearly all cases of pancreatic ductal adenocarcinoma (PDAC), yet effective clinical targeting of oncogenic KRAS remains elusive. Understanding of KRAS-dependent PDAC-promoting pathways could lead to the identification of vulnerabilities and the development of new treatments. We show that oncogenic *KRAS* induces *BNIP3L*/NIX expression and a selective mitophagy program that restricts glucose flux to the mitochondria and enhances redox capacity. Loss of *Nix* restores functional mitochondria to cells, increasing demands for NADPH reducing power and decreasing proliferation in glucose-limited conditions. Nix deletion markedly delays progression of pancreatic cancer and improves survival in a murine (KPC) model of PDAC. While conditional *Nix* ablation *in vivo* initially results in the accumulation of mitochondria*,* mitochondrial content eventually normalizes via increased mitochondrial clearance programs, and PanIN lesions progress to PDAC. We identify the Kras-Nix mitophagy program as a novel driver of glycolysis, redox robustness, and disease progression in PDAC.

Statement of significance

Nix-mediated mitophagy is a new oncogenic Kras effector pathway that suppresses functional mitochondrial content in order to stimulate cell proliferation and augment redox homeostasis. This pathway promotes the progression of PanIN to PDAC and represents a new dependency in pancreatic cancer.

Introduction

Pancreatic cancer is a deadly malignancy with a dismal 5-year survival rate of 8% (*1*). The most prevalent type, pancreatic ductal adenocarcinoma (PDAC), is characterized by near-universal mutational activation of *KRAS* (*2*). Oncogenic KRAS can promote proliferation under the nutrient-limiting conditions found in tumors by altering both the uptake of nutrients from the environment and the expression and activity of metabolic enzymes (*3-6*). *KRAS*-mutant cancer cells have also been shown to use autophagy to meet the metabolic demands of proliferation and tumorigenesis *in vitro* and *in vivo (7-10).* In these studies, pharmacological inhibition and/or genetic ablation of general autophagy and lysosomal programs led to the accumulation of defective mitochondria and consequent metabolic insufficiencies. Additionally, cells surviving loss of oncogenic *Kras* expression in an inducible model of pancreatic cancer had increased mitochondrial content and exhibited increased sensitivity to mitochondrial inhibitors (*11*). These findings suggest a possible connection between the mitochondrial content of *Kras*-mutant cells and their resultant metabolic alterations, which we hypothesized may affect tumor development *in vivo.*

Results

We previously reported that $Kras^{G12D}$ activated the Nfe2l2/Nrf2 antioxidant pathway to lower cytoplasmic reactive oxygen species (ROS), promoting cell proliferation and the initiation of early lung and pancreatic cancers (*12*). As part of these findings, we observed a $Kras^{G12D}$-dependent reduction in mitochondrial ROS levels but did not further interrogate the mitochondrial response to oncogenic Kras. Accordingly, we decided to further evaluate the acute effects of endogenous $Kras^{G12D}$ expression on the mitochondrial network using mouse embryonic fibroblasts (MEFs) and pancreatic ductal organoids generated from *LSL-*$Kras^{G12D/+}$ mice (*13, 14*). Cells were cultured in low glucose medium (0.5 mM and 2mM glucose for 2D cells and organoids, respectively), because these limited conditions select for the emergence and outgrowth of cells harboring *Kras* mutations *in vitro* and are a closer approximation than normal commercial media for the nutrient environment of PDAC *in vivo* (*15, 16*). Consistent with our published work, we found that $Kras^{G12D}$ decreased both cytoplasmic and mitochondrial ROS levels, indicated by diminished DCF-DA and MitoSox Red fluorescent intensity, respectively, in MEFs (Fig 1A). While levels of cytoplasmic ROS in *Kras*-mutant MEFs remained at *Kras*-wild type (WT) levels in the absence of Nrf2, the reduction in mitochondrial ROS persisted, suggesting that the effects of mutant Kras on mitochondrial ROS are independent of the Nrf2 program (Fig S1A). Alongside diminished mitochondrial ROS, the expression of mutant Kras in MEFs and organoids also led to decreased mitochondrial mass and total mitochondrial membrane potential per cell (Fig 1A-B), suggesting a reduced mitochondrial network. Quantification of transmission electron microscopy (TEM) images confirmed a reduction in the mitochondrial fraction of Kras-mutant MEFs and organoids (Fig 1C-D & Fig S1B-C, arrows mark mitochondria). Membrane-bound autophagosomes containing engulfed mitochondria could also be found in these micrographs (Fig S1B). Determination of the ratio of mitochondrial DNA (mtDNA) to nuclear DNA (nDNA), an alternative method of evaluating mitochondrial content, also showed a decreased ratio in $Kras^{G12D}$ MEFs compared to *Kras*-WT MEFs, further indicating a suppression of mitochondrial content (Fig S1D)(*17*).

To study the effects of loss of mutant Kras on this mitochondrial phenotype, we crossed mice harboring an excisable endogenous mutant *Kras* allele (*FRT-LSL-*$Kras^{G12V}$*-FRT*, Fig S1E) with mice harboring *LSL-*$Trp53^{R172H/+}$, *Pdx1-Cre* and *Rosa26-FlpOERT2* alleles to generate an autochthonous "FPC" mouse model of PDAC in which we could delete mutant *Kras* using tamoxifen. Cell lines derived from tumors arising in FPC mice were cultured with 4-OH-

tamoxifen (4OHT) for 96 hours, which led to excision of the mutant *Kras* allele (Fig S1F). After 4OHT treatment, FPC cells had significantly increased mitochondrial mass measured by MitoTracker Green staining (Fig 1E). Moreover, in the setting of KRAS-mutant human PDAC cell lines (Suit2 and FA6), siRNA-mediated knockdown of *KRAS* similarly led to an increase in mitochondrial mass as measured by flow cytometry, electron microscopy, and mtDNA/nDNA ratio (Fig 1F, Fig S2 A-G).

Mitochondrial mass is determined by the balance between the biogenesis of new mitochondria and the selective degradation of existing mitochondria via mitophagy (*18*). Given the increased occurrence of engulfed mitochondria that we observed in Kras-mutant organoids—and to a lesser extent in Kras-mutant MEFs—we hypothesized that mitochondrial degradation was increased in these cells. Consistent with this prediction, we did not observe significant changes in the expression of key transcription factors involved in mitochondrial biogenesis including *Pgc1a*, *Nrf1* and *Tfam* following activation of mutant Kras, suggesting that a decrease in biogenesis was not the primary explanation for decreased mitochondrial mass (Fig S3 A-B). To assess mitochondrial degradation, we first examined the expression of several mitophagy genes in $Kras^{G12D}$-expressing MEFs. In this setting, expression of $Kras^{G12D}$ resulted in increased mRNA expression of the mitophagy mediator BCL2/adenovirus E1B 19-kDa-interacting protein 3-like (*Bnip3l/Nix*) but not of other mediators of mitophagy such as p62/Sqstm1, Pink1, or Park2 (Fig S3C). Consistent with this observation, the expression of oncogenic *Kras* led to increased Nix protein in the mitochondrial fraction of MEFs without any change in the amount of p62 (Fig 2A). In organoids, we found that activation of mutant Kras also led to an increase in Nix protein and a trend towards increased *Nix* mRNA level, with a concurrent increase in levels of lipidated LC3 (LC3-II), a marker of active autophagy (Fig 2B, S3D). In parallel, the mRNA levels of *Acsm3*, a gene we previously identified as Kras-dependent in murine pancreatic organoids, increased notably (Fig S3D)(*14*). We also observed increases in both *Nix* and *p62* mRNA levels in tumor tissue isolated from the *LSL-*$Kras^{G12D/+}$*; LSL-*$Trp53^{R172H/+}$*; Pdx1-Cre* (KPC) murine model of PDAC compared with control pancreas tissue from *LSL-*$Trp53^{R172H/+}$*; Pdx1-Cre* (PC) mice, suggesting that as in MEFs, oncogenic Kras engages *Nix in vivo* (Fig S3E). Consistent with these findings, the mitochondrial fractions from a series of organoids derived from murine pancreatic intraepithelial neoplasia (PanIN, KC) and PDAC (KPC) tumors also exhibited higher levels of Nix protein compared to normal pancreas organoids (Fig 2C).

To uncover how Nix expression varies during the progression of PDA *in vivo*, we examined Nix levels by immunohistochemistry in murine normal pancreata, PanIN, PDAC, and lung metastatic lesions (Fig 2D). In this setting, we observed increased Nix staining intensity in PanIN lesions relative to normal ducts. Nix staining further intensified in PDAC and lung metastatic lesions. In contrast with the early induction of Nix, levels of p62 were not increased until later in the progression of murine PDAC, suggesting that Nix-mediated mitophagy represents a distinct pathway from p62-mediated mitophagy (Fig 2D). In agreement with our mouse IHC data, we also observed higher levels of NIX staining in human PanIN lesions compared to adjacent normal ducts as well as intense staining for NIX in human PDAC sections, suggesting that NIX induction is an early and sustained event during pancreatic tumorigenesis (Fig 2E).

To confirm that oncogenic Kras maintains Nix expression, we assessed FPC 2D cells following the deletion of $Kras^{G12V}$. Excision of mutant *Kras* led to a reduction in Nix mRNA levels and protein in FPC organoids and 2D cells, respectively (Fig 2F, S3F), demonstrating that sustained Kras signaling is required to maintain Nix levels in Kras-mutant cells. In support of this observation, we also observed decreased levels of NIX in the mitochondrial fraction of Suit2 and FA6 human pancreatic cancer cells that were treated with *KRAS* siRNA (Fig S2E-G and S3G, H). Moreover, decreased mitochondrial NIX was also observed in FA6 cells treated with either

an siRNA directed against *MAP2K2/MEK2* or the MEK inhibitor AZD6244, demonstrating a requirement for MAPK signaling through MEK downstream of oncogenic KRAS to maintain NIX levels (Fig S3G-J).

To assess the relationship between Nix expression and mitochondrial content *in vivo*, we compared Nix protein levels in the mitochondrial fraction derived from the pancreata of WT mice and PanIN-bearing KC mice and observed higher levels of Nix protein in KC pancreata compared to WT controls (Fig 3A and S4A). To gauge mitochondrial content, we isolated DNA from these pancreata and determined the ratio of mtDNA to nDNA (Fig 3B). As in our *in vitro* experiments, the mtDNA/nDNA ratio for KC pancreata was significantly lower than that of WT pancreata and showed an inverse relationship with the amount of Nix protein in the mitochondrial fraction of the tissue, confirming that increased Nix levels are associated with less mitochondrial content *in vivo* (Fig S4B).

Building upon these observations, we sought to confirm whether Nix-mediated mitophagy is responsible for the suppression of mitochondrial content observed after mutant *Kras* expression *in vitro* and *in vivo*. To this end, we assessed mitochondrial mass in Kras-mutant MEFs and in two KRAS-mutant human PDAC cell lines following siRNA-mediated depletion of NIX. In Kras-mutant MEFs, *Nix* knockdown led to increased mitochondrial mass, mitochondrial ROS, and mitochondrial membrane potential compared to Kras-mutant cells treated with control siRNA (Fig 3C). Similar results were observed following *NIX* knockdown in FA6 and Suit2 cells (Fig 3D). These changes were also recapitulated in both MEFs and FA6 cells treated with the MEK inhibitor AZD6244 (Fig S4 C-D) as well as in FA6 cells treated with siRNA against MAP2K2/MEK2 (Fig 3E), confirming that MAPK signaling is important for maintaining both Nix and the mitophagy program. In the human cancer cell lines, these findings were further validated by confirming that siRNA depletion of NIX increased both the mitochondrial fraction in TEM images and the mtDNA/nDNA ratio of the siNIX cells compared with controls (Fig S2A-C), similar to the changes observed following the knockdown of *KRAS* in these cells.

Because NIX is known to be a facilitator of mitophagy and higher NIX levels correlated with reduced mitochondrial mass across our experimental systems, we sought to confirm whether perturbing NIX would alter mitochondrial flux in Kras-mutant cells(*19, 20*). We generated FA6 and Suit2 cells that stably express the mitoQC mitophagy probe (FA6-mtQC and Suit2-mtQC), a mitochondrially-targeted tandem GFP-mCherry probe that allows for analysis of relative mitophagic flux(*21*). In cells expressing the probe, mitochondria will exhibit dual mCherry and GFP fluorescence at steady state while those mitochondria found within lysosomes, i.e. mitochondria undergoing mitophagy, will lose GFP fluorescence, which is quenched in an acidic environment. In an analogous way to the tandem LC3 general autophagy probe and the mt-Keima mitophagy probe, the ratio of mCherry to GFP mitoQC fluorescence as determined by flow cytometry can reveal differences in mitophagic flux (*22, 23*). NIX-depleted FA6-mtQC and Suit2-mtQC cells showed a modest reduction in their mCherry/GFP ratios compared with control cells, consistent with decreased mitophagic flux in these cells (Fig S4E-F). In comparison, knockdown of p62 led to greater suppression of mitophagy in both FA6 and Suit2 cells, likely reflecting p62's more expansive role as a mediator of various selective autophagy programs, including the PINK-PARKIN-p62 mitophagy program, which can clear damaged mitochondria independently of NIX (*18*) (Fig S4E-F).

In glucose-limited environments, suppression of mitochondrial content and mitochondrial network activity could act to directly limit the amount of glucose available for mitochondrial oxidative phosphorylation. In such a model, mitophagy would divert glucose away from the tricarboxylic acid (TCA) cycle and allow for its greater utilization in aerobic glycolysis and other anabolic pathways. Such channeling of glucose to lactate could also support the high level of NAD+ generation required to maintain the elevated glycolytic rate of cancer cells(*24*). Since it

has been shown that *KRAS* mutations provide a growth advantage to cells cultured in glucose-limited medium (*15*), we investigated whether the KRAS-NIX mitophagy program might support increased proliferation in these conditions. In agreement with this hypothesis, we found that although siRNA-mediated depletion of NIX in both FA6 and Suit2 cells did not alter proliferation in high glucose (25 mM glucose) media, proliferation was reduced in low glucose (0.5 mM glucose) conditions (Fig 3F). This proliferative defect following Nix loss was even more profound in $Kras^{G12D}$-expressing MEFs and occurred even in high glucose conditions (Fig S4G).

Oncogenic RAS has been previously reported to engage a p62-dependent autophagy program that is required for pancreatic cancer progression (*7, 25*). This requirement for p62 in RAS mutant cells may reflect both its central function in selective autophagy/mitophagy programs and subsequent maintenance of a pool of functional mitochondria (6) as well as its function in promoting Nrf2 anti-oxidant signaling through interactions with Keap1 (*26*). As such, we considered whether the Nix program might similarly prevent the accumulation of damaged mitochondria or instead reduce pools of functional mitochondria – a phenomenon reported during red blood cell development (*19, 20*). To assess whether mitochondria restored by the loss of Nix in *Kras-mutant* cells were functional, we measured the oxygen consumption rate (OCR) following constitutive knockdown of *Nix* in mouse tumor (mT) organoids, $Kras^{G12D}$-expressing MEFs, and human PDAC cells. In organoids, shRNA-mediated knockdown of *Nix* led to increased basal respiration and a greater maximal respiratory rate in response to the mitochondrial uncoupler FCCP, suggesting that restored mitochondria in organoids are indeed functional (Fig 4A). Similarly, in $Kras^{G12D}$-expressing MEFs and in Suit2 and FA6 cells, *NIX* knockdown increased basal and maximal respiratory capacity (Fig S5A and 4B, respectively). To further interrogate the functional state of mitochondria restored to NIX-depleted cells, we quantified the number of cristae per mitochondrion in our TEM images of Suit2 and FA6 cells following NIX depletion. A decrease in this metric has been shown to correspond with faulty mitochondrial function (*27, 28*). Consistent with the mitochondria in siNIX cells being functional, we did not detect significant alterations in cristae per mitochondrion in siNIX cells (Figure 4C-D). Similarly, we found that although mitochondrial ROS per cell increased after NIX knockdown *in vitro* (Fig 1A and 3D), the mitochondrial ROS per mitochondrial mass ratio did not increase as would be expected if the mitochondria were damaged (Figure 4E). We then challenged cells with the mitochondrial-specific ROS inducer mitoParaquat (mitoPQ) ((*29*)) to see if mitochondria in NIX-depleted cells were more sensitive. As expected, acute treatment with mitoPQ increased the mitochondrial ROS/mass ratio compared to control treated cells (Figure S5B). However, this occurred to a similar extent independently of the NIX status of the treated cells, suggesting that the mitochondria in NIX-depleted cells were not more sensitive to the treatment. Finally, we cultured FA6 and Suit2 cells in galactose media, an environment where mitochondrial function is required in order to generate ATP from galactose (*30*). Intriguingly, we observed increased proliferation in the NIX-depleted cells compared with controls (Figure 4F), supporting our conclusion that the KRAS-NIX mitophagy program clears otherwise functional mitochondria.

Given that an increased mitochondrial network might consume greater amounts of available cellular glucose, we evaluated whether $Kras^{G12D}$-driven mitophagy reduces mitochondrial glucose flux. Consistent with this hypothesis, we observed smaller steady state pools of the TCA cycle intermediates succinate and malate in $Kras^{G12D}$ MEFs compared with WT MEFs, with a restoration of these pools to WT levels in $Kras^{G12D}$ MEFs treated with Nix siRNA (Fig 4G). In agreement with this observation, siRNA-mediated NIX depletion in both FA6 and Suit2 cells led to greater accumulation of $^{13}C_6$-glucose-derived label in TCA cycle intermediates, especially citrate and malate, following a 45 minute incubation with 2mM $^{13}C_6$-glucose, with comparable labeling of glycolytic pools of glucose 6 phosphate (G6P), dihydroxyacetone phosphate/glyceraldehyde-3-phosphate (DHAP/G3P), and pyruvate (Fig 4H,

S5C-E). Although the intracellular lactate pool modestly increased in siNIX cells, relative partitioning of glucose label between citrate in the TCA cycle and lactate, as judged by the citrate m+2 / lactate m+3 ratio, was increased (Figure 4I, S5F). To further interrogate glucose flux in response to perturbing Nix in a more physiologically relevant 3-dimensional setting, mT organoids were cultured with 2mM uniformly labeled $^{13}C_6$-glucose for 45 minutes, and glucose metabolism via glycolysis and the TCA cycle was analyzed. Both constitutive knockdown of *Nix* in mT8 organoids and its inducible knockdown in mT5 organoids led to a significant increase in the accumulation of labeled isotopologues of TCA cycle intermediates in shNix organoids compared with controls (Fig S5G-I). As in the 2D cells, increased glucose flux into the TCA cycle correlated with reduced relative glucose flux to lactate (Fig S5J-K). These findings demonstrate that suppression of mitochondrial content in $Kras^{G12D}$ –expressing cells facilitates reduced cycling of glucose-derived carbon within mitochondria and its greater relative conversion to lactate.

Previous studies have demonstrated that pancreatic cancer cells upregulate the non-oxidative arm of the pentose phosphate pathway (PPP) to generate nucleic acids while relying on the Nrf2 antioxidant program to limit intracellular ROS (*4, 12*). Tracing experiments with 2mM $^{13}C_6$-glucose demonstrated that NIX depletion led to greater flux from glucose to ribose phosphate (R5P) through the pentose phosphate pathway in our organoid and 2D cultured cells during the 45 minute labeling period (Fig 4H, S5D,H,I). Given that siNIX cells have higher levels of mitochondrial ROS, we predicted that the observed increased glucose flux to R5P might be through the oxidative arm of the PPP to generate NADPH. To test this idea, we incubated FA6 cells for three hours with 2mM 1-$^{13}C_1$-glucose, a glucose isotopologue that can be used to distinguish between the oxidative and non-oxidative routes through the PPP to form R5P (Fig S6A). In this experiment, the ^{13}C label is retained on R5P if glucose is metabolized through the non-oxidative branch of the PPP but is lost if it instead traverses the oxidative arm of the PPP. Thus, the relative m+0/m+1 ratio of labels in ribose-5-phosphate reflects the contribution of oxidative versus non-oxidative PPP activity in the cells(*31*). In unstressed conditions, FA6 siNIX cells exhibited a larger m+0/m+1 ratio than NT controls, suggesting greater basal requirements for oxidative PPP flux (Fig 4J) - albeit in maintenance of a more oxidized baseline NADPH/NADP+ redox ratio (Fig 4K). This finding generalized to both Suit2 cells and organoids wherein NIX depletion resulted in reduced steady-state NADPH/NADP+ ratios in each system (Fig 4L/M). In the FA6 cells, applying redox stress using menadione further increased flux through the oxidative branch of the PPP independently of NIX status, as expected, but to a greater extent in siNIX cells, underscoring their increased redox burden (Fig 4J-K).

PDAC cells have been shown to largely use glutamine to fuel their TCA cycle(*3*). As such, we investigated whether NIX-depletion also altered glutamine flux by incubating cells for 45 minutes with 2mM uniformly carbon- and nitrogen-labeled ($^{13}C_6$,$^{15}N_2$) glutamine (Fig S6B). Consistent with our glucose tracing experiments, upon knockdown of Nix in FA6 and Suit2 cells and organoids, we observed increased TCA accumulation of glutamine label (Fig S6C-F). Malic enzyme activity, in addition to oxidative PPP activity, can generate NADPH and has been shown to be important in PDAC(*3, 32*). Malic enzyme activity can be inferred by examining the generation of m+3 pyruvate from glutamine-labeled malate (Fig S6G). In glutamine-labeled PDAC cells and organoids depleted of NIX, however, we did not observe significantly different accumulation of m+3 pyruvate between conditions—although labeling of m+3 pyruvate in each case was low, as also reported by Son *et al* (*3*)—suggesting that malic enzyme activity was similar (Fig S6C-F). Increased reductive carboxylation has been revealed as a strategy used by non-adherent cells to cope with redox stress (*33*). In non-adherent cells, reductive carboxylation of glutamine to citrate followed by its subsequent oxidation in the mitochondria acts to shuttle reducing equivalents from the cytosol to the mitochondria. In the FA6 cells and both organoid systems, we found that reductive carboxylation of glutamine to citrate, as judged by the

m+5/m+4 citrate ratio in glutamine labeled cells(*34*), increased upon Nix knockdown (Fig S6B,S6H-K). In Suit2 cells, this was not the case, although these cells had by far the highest levels of m+5 citrate label accumulation independently of NIX status (Fig S6D), suggesting that reductive carboxylation of glutamine to citrate is already occurring at high levels in these cells. The reductive carboxylation of glutamine to citrate can act to shuttle NADPH reducing equivalents to the mitochondria as follows: NADPH is first consumed by cytoplasmic IDH1 to make citrate from aKG. As long as mitochondria are functional, the subsequent oxidation of this citrate then regenerates NADPH in the mitochondria (*33*). Redox cycling through the pathway can be inferred by determining if citrate continues oxidatively to malate, yielding m+4 malate (and mitochondrial NADPH) or proceeds reductively, yielding m+3 malate (but no mitochondrial NADPH) (Fig S6G). We did not observe a decrease in the malate m+4/m+3 ratio in any of the cell types tested, as occurs in hypoxia when cells suppress mitochondrial oxidation activity, and even observed an increase in the ratio in Suit2 cells (Fig S6L-O) (*35, 36*). This shows that NIX-depleted cells are capable of completing the NADPH shuttle. Considered alongside our other data, we believe this finding suggests that NADPH shuttling may help to augment mitochondrial redox control in NIX-depleted cells. Taken together, our results suggest that the greater mitochondrial ROS production associated with the increased functional mitochondrial pool in NIX-depleted cells increases their requirement for oxidative PPP flux to generate NADPH. Some of these reducing equivalents may then be shuttled to mitochondria via increased reductive carboxylation of glutamine to citrate.

To determine whether the Nix-mediated mitochondrial and metabolic alterations observed *in vitro* influence the development of pancreatic cancer, we conditionally deleted Nix in the pancreata of KC and KPC mice using a floxed *Nix* allele (*37*). At 3 months of age, KCNix$^{FL/FL}$ (KCNix$^{\Delta/\Delta}$) mice formed low-grade PanIN-1A lesions similar to KC mice (Fig S7A). We confirmed that Nix was deleted throughout the exocrine pancreas compartment in these mice (i.e. acinar cells and ductal cells) with expression retained in cells of other lineages (i.e. fibroblasts and immune cells) (Fig S7B). Despite Nix deletion, PanIN-1 lesions in KCNix$^{\Delta/\Delta}$ mice had similar levels of Ki67 and p-Erk expression compared to controls (Fig S7B), suggesting that loss of Nix did not initially impair the proliferative effects of oncogenic Kras signaling. Nonetheless, by later time points (9-12 months) when all KC mice harbored extensive PanIN lesions and possessed little normal tissue, KCNix$^{\Delta/\Delta}$ mice retained a significantly larger fraction of disease-free normal pancreas tissue, demonstrating a delay in PanIN progression (Fig 5A-B). Indeed, although all KC mice examined harbored PanIN-2 and PanIN-3 lesions, most KCNix$^{\Delta/\Delta}$ mice still exhibited only low-grade PanIN-1A and PanIN-1B lesions (Fig 5C-D). Extending these observations to the aggressive KPC genetically engineered mouse model of PDAC, the pancreata of *KPCNix$^{FL/FL}$* (KPCNix$^{\Delta/\Delta}$) mice sacrificed at 4 months had mostly low-grade PanIN-1A and PanIN-1B lesions, with only 1 mouse (out of 5 mice analyzed) harboring a solitary cystic papillary neoplasm (CPN), and no mice harboring PDAC within the cohort (Fig 5E-F). In age-matched KPC mice, PDAC was observed in 60% of KPC mice and all mice showed at least PanIN-2 lesions (Fig 5E-F).

Given the differences that we observed in PanIN progression to PDAC in both KC and KPC pancreatic cancer models with *Nix* deletion, we decided to examine whether this delay also correlated with increased survival within the KPC model. We first confirmed that mitochondrial content was disrupted in KPCNix$^{\Delta/\Delta}$ mice. As expected, 16-week-old KPCNix$^{\Delta/\Delta}$ mice exhibited increased mitochondrial content in PanIN lesions as judged by the immunofluorescent detection of Tom20, a mitochondrial marker (Fig 6 A-B). We followed a cohort of mice to humane endpoint and found that *Nix* ablation in the KPC model led to a significant extension of median survival from 21.86 weeks to 34.86 weeks in KPCNix$^{\Delta/\Delta}$mice, although KPCNix$^{\Delta/\Delta}$ mice eventually all succumbed to malignant disease (Fig 6C). Interestingly, analysis of The Cancer

Genome Atlas (TCGA) data from resected PDAC patients showed that elevated *NIX* mRNA expression was associated with significantly shorter survival in humans as well (Fig 6D). Even though Nix loss was maintained in PDAC tumors from KPCNix$^{\Delta/\Delta}$ mice (Fig S8A), the mitochondrial content in PDAC lesions of KPC and KPCNix$^{\Delta/\Delta}$ mice had normalized by survival endpoint (Fig 6E-F), suggesting that PDAC tumors in KPCNix$^{\Delta/\Delta}$ mice had acquired the ability to overcome deficits in the Nix mitophagy program. This observation was recapitulated in organoids derived from KPC and KPCNix$^{\Delta/\Delta}$ mice grown in low glucose medium, wherein mitochondrial content in the groups was not significantly different—confirming a selective pressure to maintain mitochondrial content suppression in Kras-mutant cells (Fig S8B-C). We hypothesized that the normalization of mitochondrial content by survival endpoint might reflect compensatory upregulation of autophagy or mitophagy pathways. Indeed, in two out of three organoid lines derived from KPCNix$^{\Delta/\Delta}$ mice at survival endpoint, we found elevated levels of Bnip3, a hypoxia-inducible mitophagy adaptor protein (Figure 6G). The third KPCNix$^{\Delta/\Delta}$ organoid line expressed lower levels of Bnip3, however, upon addition of chloroquine, this line demonstrated increased accumulation of LC3-II, indicating increased autophagic flux (Fig S6G). Additionally, when Suit2 and FA-6 cells were grown in low glucose media in hypoxic (1% O_2) culture conditions, knockdown of Nix led to induction of Bnip3 and loss of the proliferation defect seen in normoxic low glucose conditions (Fig S8D-E). Similarly, in a panel of organoids derived from 16-week-old KPC and KPCNix$^{\Delta/\Delta}$ mice, hypoxic conditions led to an induction of Bnip3 in Nix-null organoids, possibly as a compensatory mechanism for Nix-null cells to adapt to hypoxic conditions like that characteristic of the PDAC microenvironment (Fig S8F). Staining of tumor sections revealed that a greater fraction of KPCNix$^{\Delta/\Delta}$ tumors had high positivity of Bnip3 staining compared to KPC controls (Fig 6H-I), supporting our *in vitro* findings that Nix ablation was accompanied by upregulation of Bnip3. Collectively, our results demonstrate that Nix promotes the progression of Kras^{G12D}-driven PanIN to PDAC and nominate the Nix pathway as a new dependency in PDAC.

Discussion

General autophagy has previously been shown to support a glycolytic metabolic shift during Ras-driven cellular transformation (*38, 39*). More recently, selective mitophagy has been implicated as a driver of glycolysis in the setting of normal physiological development (*39*). Here, we present evidence that Kras-mutant cancer cells can channel their glucose metabolism away from the mitochondria by a previously unappreciated means: programmed mitophagy via the mediator BNIP3L/NIX. We find that oncogenic Kras induces Nix expression and suppression of mitochondrial content in a MAPK pathway-dependent fashion. Loss of Nix led to a shift toward oxidative glucose metabolism, with a compensatory increase in flux through the oxidative arm of the PPP and reductive carboxylation of glutamine—pathways that regenerate NADPH and can facilitate its shuttling into mitochondria. Since we did not analyze mitochondrial NADPH levels directly, more work will be required to confirm the importance of redox shuttling for mitochondrial redox homeostasis in NIX-depleted cells. *In vivo,* Nix ablation led to an increase in mitochondrial content within PanIN lesions and a delay in progression of these pre-malignant lesions to higher grade PanIN and to *bona fide* PDAC.

The role of selective autophagy has been less well studied than that of general autophagy in PDAC. Studies of the Pink/Parkin pathway and Bnip3 suggest that these pathways can have tumor suppressive functions as well as mitophagy-independent activities in various cancer types (*18, 40*). In the KC mouse model, for example, conditional deletion of either Pink1 or Park2 was shown to lead to shorter survival and increased invasiveness of tumor cells, while high mRNA expression of PRKN/PARK2 correlates with improved survival in human patients (*40*). Cancer cells from KC mice lacking Pink1 or Park2 demonstrate increased mitochondrial

iron accumulation and increased lactate production in a Hif1α-dependent manner both *in vivo* and *in vitro.* Similarly, deletion of Bnip3 in breast cancer cells leads to upregulation of glycolysis and promotes tumor progression(*41*). Studies examining the role of Nix in cancer have also suggested a putative role as a tumor suppressor in certain contexts (*18, 42-44*). Instead, we find that in Kras-mutant pancreatic cancer cells, Nix serves to suppress mitochondrial ROS production by decreasing the mitochondrial network, augmenting redox robustness and allowing for increased glycolytic metabolism of glucose to lactate—similar to the metabolic switch observed in red blood cell maturation (*39*). These activities promote development of PDAC from PanIN lesions. In the KC and KPC mouse models, the role of Nix is pro-tumorigenic as Nix ablation significantly delays tumor progression and extends survival. Additionally, elevated expression of Nix mRNA within a cohort of PDAC patients from the TCGA correlates with significantly worse survival. Together, our results demonstrate how Nix-mediated programmed mitophagy may play a distinct and possibly opposing role to the traditional damage-control selective autophagy response (i.e. through Pink1/Park2 or Bnip3) to mediate metabolic transformation and promote pancreatic cancer.

Intriguingly, we observed that the mitochondrial content of tumors in Nix knockout mice at clinical endpoint was comparable to that within KPC controls, as was also seen in the organoids derived from these tumors after culture *in vitro*. The observed normalization of mitochondrial content *in vivo* and *in vitro* paralleled a compensatory upregulation of Bnip3 or general autophagy flux in organoids derived from Nix-deficient tumors, presumably to maintain a preferred reduced mitochondrial set point. In addition to this apparent compensation, it is also possible that some of the observed equalization of mitochondrial content may represent expansion of the mitochondrial network during disease progression within the KPC (Nix WT) tumors themselves. Increased mitochondrial biogenesis, for example, driven by Myc and other oncogenic transcription factors, has been shown to be engaged to support increased metabolic demands during tumor development (*45*) and might act to counter mitochondrial suppression as KPC tumors progress.

We found that loss of Nix restores functional mitochondria to pancreatic cancer cells, leading to increased respiratory capacity in these cells and a reduced ability of resultant PanIN lesions to progress to cancer *in vivo.* Our findings are in line with a recent analysis of an siRNA screen that found increased expression of general autophagy pathways and Nix among KRAS-dependent human cancer cell lines in comparison to their KRAS-independent counterparts (*46*). In this analysis, the KRAS-dependent cell lines tended to be more glycolysis-dependent, supporting the notion that Nix may be important for driving KRAS-mediated metabolic transformation (*46*). Decades ago, a debate arose questioning whether cancer cells that metabolize glucose through aerobic glycolysis exhibit “impaired respiration” and whether this metabolic shift is an initiating event in tumorigenesis (*47-49*). More recently, several studies have demonstrated that KRAS-mutant cells do indeed require mitochondrial function to metabolize glucose, glutamine, and lactate, and to support tumorigenesis (*3, 7, 50, 51*). Despite our observation that conditional deletion of Nix initially delays PDAC development, we find that, consistent with those previous studies, conditional Nix knockout mice still eventually succumb to malignant disease. Additionally, our findings suggest that therapeutic targeting of mitophagy in combination with ROS-generating compounds may lead to new possibilities for the treatment of PDAC and other Kras-mutant cancers.

Acknowledgments:
We thank Dr. Gerald Dorn for kindly providing the Nix^{FL} mouse strain. We thank Dr X. Zou for assistance in generating the FRT-LSL-KrasG12V-FRT mouse. We thank Dr. Stephen Tait for providing the mitoQC construct and Dr. Richard Hartley for providing the mitoPQ control compound. We also acknowledge the Cold Spring Harbor Laboratory Animal and Genetic Engineering, Animal and Tissue Imaging, Microscopy, Flow Cytometry core facilities, which are funded by the NIH Cancer Center Support Grant 5P30CA045508. We thank Susan Van Horn and the Stony Brook Central Microscopy Imaging Center for assistance with electron microscopy of organoids. We also acknowledge the Metabolomics facility and Cancer Metabolism Research Unit at the CRUK Beatson Institute and thank G. Mackay and D. Sumpton for their assistance and advice. We thank Dr. L. Baker for her critical reading of the manuscript. We thank members of the D. Tuveson Lab, N. Sodir and other members of the G. Evan lab, and C. Labuschagne, A. Hock, M. Yang, and other members of the K. Vousden lab for their assistance and advice.

Funding:

DAT is a distinguished scholar of the Lustgarten Foundation and Director of the Lustgarten Foundation-designated Laboratory of Pancreatic Cancer Research. DAT is also supported by the Cold Spring Harbor Laboratory Association, the V Foundation, and the National Institutes of Health (NIH 5P30CA45508, 5P50CA101955, P20CA192996, 1U10CA180944, U01CA224013, U01CA210240-01A1, 1R01CA188134, and 1R01CA190092). BA is supported by NCI 5F30CA200240. YP is supported by R50CA211506. GY is supported by a Boehringer Ingelheim Fonds Fellowship. KFM is supported by NIH/NCI RO1 CA200310 and RO1 CA216242. MPM is supported by Medical Research Council UK (MC_UU_00015/3) and by a Wellcome Trust Investigator award (110159/Z/15/Z). TJH and KHV are supported by Cancer Research UK and by ERC grant 322842-METABOp53. TJH was also supported by the Gates Cambridge Trust. GIE and DL are supported by Cancer Research UK Programme Grant A12077 (P.I. Evan) - "Deconstructing Myc oncogenesis".

Authors contributions:
TJH, BA, and DAT conceived the project and wrote the manuscript. GMD assisted in labeled glucose and glutamine metabolomics experimental designs and the interpretation of these results. DL contributed to the design and optimization of steady-state GC–MS experiments. KHV contributed to the interpretation of LC-MS labeling experiments. PP-M created the Frt-LSL-$Kras^{G12V}$-FRT targeting vector and mouse. TJH and BA performed all other experiments and data analysis with assistance from GNY, MAY, CSL, PA, MNZ, and YP. All of the authors discussed the results and commented on the manuscript.

Data and materials availability:
All data are presented in the main text and supplementary materials.

Materials and Methods

Generation of FRT-LSL-Kras^{G12V}-FRT knock-in mice

A fragment of the murine *Kras* genomic locus harboring Exon1 was cloned in pBluescript. Next, a Gly (GGT) to Val (GTT) substitution was introduced in codon 12. Finally, a FRT-LoxP-STOP-LoxP cassette was cloned upstream the Exon1^{G12V}, and an additional FRT site cloned downstream the Exon1^{G12V}. TL1 ES cells (*52*) were electroporated with the linearized pBluescript-FRT-LSL-Kras^{G12V}-FRT targeting construct, and correctly targeted puromycin-resistant clones were identified by Southern blot. Two positive clones exhibiting a normal karyotype were used to generate chimeric mice by microinjection into C57BL/6 blastocysts. Germline transmission of the targeted allele was confirmed by Southern blot analysis of tail DNA from the agouti offspring.

Mice

All animal experiments were reviewed and approved by the IACUC of Cold Spring Harbor Laboratory. The *LSL-Kras^{G12D}; LSL-Trp53^{R172H}; Pdx1-Cre* and *Nix^{FL}* strains have been described previously (*13, 37, 53*). Animals were maintained on a C57Bl6/J background backcrossed at least 10 generations. The number of animals used in each experiment is stated in the figure legends.

Human PDAC tissue

Resected pancreatic cancer specimens were obtained as excess tissues from Johns Hopkins University following on an IRB approved protocol. Tissue was fixed in formalin and processed for IHC as described below.

Immunohistochemistry and Immunofluorescence

Tissues were fixed in 10% Neutral Buffered Formalin for 24 hours before paraffin-embedding and sectioning. Slides cut from paraffin blocks were de-paraffinized and rehydrated. Antigen retrieval was performed in 10 mM citrate buffer (pH 6) for 6 minutes in a pressure cooker. For immunohistochemical staining, endogenous peroxidase activity was quenched by incubation in 3% hydrogen peroxide for 15 minutes followed by rinsing in water and blocking in 2.5% normal horse serum. Slides were incubated with primary antibody diluted in blocking solution overnight at 4°C. Secondary antibody (Vector Immpress) was used according to manufacturer's instructions followed by development using DAB (Vector). Slides were dehydrated and mounted with coverslips and imaged using a Zeiss microscope. For immunofluorescent staining, following antigen retrieval, sections were blocked in 2.5% normal horse serum before incubation in primary antibody diluted in 5% BSA in TBST overnight at 4°C. Secondary antibody and DAPI were diluted in 1% BSA in PBS and added to sections for 1 hour in the dark before mounting with cover slips. Antibodies used: Nix (#12396, Cell Signaling Technology), p62 (Enzo), p-ERK1/2 (#4370, Cell Signaling Technology), Tom20 (#42406, Cell Signaling Technology), Ki-67 (RM-9106, Thermo), Bnip3 (Sigma).

Analysis of H&E-stained pancreata

Blocks were serially sectioned for 80 sections and H&E staining was performed on every fifth and sixth section. H&E sections were evaluated for highest grade lesion present in a blinded fashion. H&E sections of pancreata from 9-12-month-old KC mice were scanned using an Aperio scanner and image analysis was performed using AperioImageScope v11.2.0.780. To determine the area of normal pancreas, the Positive Pixel Count v9 macro was used with the following parameters: Hue value (0.006), Hue width (0.5), Color Saturation Threshold (0.27), Upper pixel threshold value (220), Lower pixel threshold value (0). To find the fraction of normal

pancreas, the total number of positive pixels were divided by the total number of pixels (Positivity output).

Analysis of IF images

Pan-IN lesions were imaged on a LSM 710 Confocal Microscope (Zeiss) at 63x magnification. Tumor sections were imaged on a SP8 confocal microscope (Leica) at 40x magnification. ImageJ v.1.51n was used for all image analyses. To find the total mitochondria area, images were first processed by applying a Gaussian Blur (sigma=0.5). To separate the true mitochondrial staining from background the images were then made binary by using the same pixel intensity threshold for all images within an experiment. To calculate the total area of all mitochondria, the 'Analyze particles' function was used to count all objects. Nuclei were counted using the 'Analyze particles' function and objects of size 50 to infinity were counted. Manual segmentation of adjacent nuclei was done as needed.

Cells, cell culture, and organoid culture

MEFs were generated and maintained as previously described(*12*). MEFs were used at early passage for every experiment but were not tested for mycoplasma at any point. Human PDAC FA-6 (CVCL_4034) and Suit2 (CVCL_3172) cells were originally obtained from Clare Hall Laboratories (CRUK). Human cell lines were periodically tested for mycoplasma and confirmed as mycoplasma negative using the MycoAlert Mycoplasma Detection Kit (Lonza LT07-318), most recently after re-submission experiments. Cell line authentication was not performed. 2D FPC cancer cell lines were generated from FPC mice as previously described (*54*). Mouse organoids and 2D mouse cancer cell lines were tested for mycoplasma at least once after isolation or thawing and were re-tested prior to performance of metabolomics and flow cytometry experiments using the MycoAlert Mycoplasma Detection Kit (Lonza LT07-318). All experiments were performed on organoids/cell lines cultured for fewer than 15 total passages.

MEFS, human PDAC cell lines (Suit2, FA6), and mouse cancer cell lines were maintained in DMEM (Gibco, 21969) containing 25 mM glucose and supplemented with 2 mM glutamine, 1% Penicillin/Streptomycin, and 10% FBS. When indicated, 2D experiments were performed in low glucose medium (glucose-free, pyruvate-free, glutamine-free DMEM (Gibco A1443001) supplemented with 10% FBS, 0.5 mM glucose, 2 mM glutamine, and 1% Penicillin/Streptomycin). MEK inhibitor experiments used AZD6244 at a concentration of 5 μM and treated for 24hrs. Galactose proliferation experiments were performed in Galactose media (glucose-free, pyruvate-free, glutamine-free DMEM (Gibco A1443001) supplemented with 10% FBS, 5g/L galactose (Sigma), 2 mM glutamine, and 1% Penicillin/Streptomycin). For induction of mitochondria targeted ROS, mitoPQ (Abcam) or carrier (control) was added to media at 5uM for 20 minutes.

Organoids were generated and cultured as previously described (*14*). Briefly, organoids grown in reduced growth factor Matrigel (Corning) were removed from Matrigel by incubating with 2 mg/mL of Dispase at 37°C. Isolated organoids were dissociated using TrypLE Express (Gibco) and the resultant single cells were counted and plated as for experiments as described elsewhere. When indicated, organoids experiments were performed in low glucose medium: glucose-free, pyruvate-free Advanced DMEM/F12 supplemented with 2mM glucose and growth factors as described previously with the exception of R-spondin-conditioned medium, Epidermal growth factor, and N-acetyl-cysteine, which were excluded (*14*). For autophagy flux experiments in organoids, chloroquine (Sigma, 25uM) or vehicle control was added to media for 24 hours.

Adeno-Cre and Retroviral infections

Retroviral and adenoviral infections were performed on MEFs and organoids as described previously (*12, 14*). Briefly, dissociated organoids were resuspended in Advanced DMEM/F12 (plus 1% Penicillin/Streptomycin, 2 mM Glutamax and 1 mM HEPES pH 7.2-7.5; "+++ medium") containing retrovirus or adenovirus (500 pfu/cell) and centrifuged for 1-2 hours at 800 g. Antibiotic selection of retrovirally-infected organoids (puromycin 2 μg/mL) was performed for at least 48 hours.

shRNAs were chosen from a published library and cloned into the LEPG and RT3GEPIR vectors as previously described (*55*). Cells infected with hairpins cloned into the tet-inducible RT3GEPIR vector were treated with doxycycline (1 μM) for 72 hours prior to experimental analysis unless otherwise stated. The following shRNA target sequences were used:

Renilla Luciferase 713: TGCTGTTGACAGTGAGCGCAGGAATTATAATGCTTATCTA
TAGTGAAGCCACAGATGTATAGATAAGCATTATAATTCCTATGCCTACTGCCTCGGA

Mouse Nix 447: TGC TGT TGA CAG TGA GCG ATC AGA AGA AGA AGT TGT AGA ATA GTG AAG CCA CAG ATG TAT TCT ACA ACT TCT TCT TCT GAC TGC CTA CTG CCT CGG A

siRNA transfections

ON-TARGET*plus* SMARTpool siRNA (Dharmacon / Thermo Scientific) was used for all siRNA knockdown experiments. Cells were transfected with the selected ON-TARGETplus SMARTpool siRNA constructs (25 nM final concentration), DharmaFECT 1 reagent (Thermo Scientific), and Opti-MEM (Life Technologies) according to Thermo Scientific's recommendations.

The following Dharmafect siRNA targets were used:
Non-targeting control (cat # D-001810-10-05)
Human KRAS (cat # L-005069-00-0005)
Human NIX / BNIP3L (cat # L-005069-00-0005)
Human MAP2K2 / MEK2 (cat # L-003573-00-0005)
Human p62 / SQSTM1 (cat # L-010230-00-0005)
Mouse Nix / Bnip3l (cat # L-058953-00-0005)

Cell Proliferation

MEFs were infected with adenoviral control or CRE at least 72 hours prior to transfection with siRNA. At the start of the experiment, both MEFs and human cells were seeded into three wells each on duplicate 6 well plates per condition ($1*10^5$ cells per well for MEFs and $7.5*10^4$ cells per well in human cells). The following day, cells were transfected with indicated siRNA constructs and left in 25mM glucose DMEM media overnight. At this point, one plate of the triplicate wells was counted to determine Day 0 counts. On the second plate, media was either replenished with 25mM glucose DMEM or switched to low glucose DMEM. Media was changed for a second time on day 2. These plates were counted either 3 or 4 days later as indicated, and the resulting ratios to the Day 0 counts compared.

For the hypoxia proliferation comparison in figure S8, we utilized FA6 cells that stably express pBabe-iRFP-PURO, generated as previously described for HCT116 cells(*56*). Otherwise, the cells were treated the same as in other experiments, shifted to ± 1% oxygen conditions at 24 hrs post-transfection (when they were also shifted to low glucose media). Instead of counts, the Day

4 iRFP intensity values were compared across conditions after confirming that the Day 0 initial scans of each well all had similar values.

Oxygen Consumption Measurement
Dissociated organoids were plated as 10,000 single cells in 2.5 microliter domes of Matrigel (Corning) in XF96 assay plates (Agilent) and cultured in low glucose medium for 48 hours prior to assay. Domes were overlaid with 180 microliters of low glucose medium. Adherent cells were first transfected with indicated siRNA constructs and cultured for 48 hours before being seeded at $2*10^4$ cells / well in XF96 plates and cultured for an additional two days in low glucose medium. Mito Stress test assays were performed according to manufacturer's instructions using oligomycin (1 μM), FCCP (1 μM), and rotenone/antimycin A (0.5 μM/ 0.5 μM) with 3-4 measurement cycles before and after each injection.

Transmission Electron microscopy
Human cells were transfected with indicated siRNA constructs and MEFs infected with adenoviral control or CRE, and cells were cultured for an initial 48 hours post-infection/transfection. MEFs and Human 2D cells were cultured in low glucose (0.5 mM) DMEM medium for 48 hours prior to fixation (96 hours post-infection/transfection). Cells were washed in ice-cold saline (0.9% NaCl) and fixed in an ice-cold solution of 2% glutaraldehyde and 2% formaldehyde in 0.5M sodium cacodylate buffer (pH 7.4) for 4 hours at 4°C. The cells were then washed in 0.1M sodium cacodylate buffer five times, treated with 1% Osmium ferricyanide at 20°C for 2 hours, washed five times in de-ionized water, and treated with 2% uranyl acetate in 0.05 M maleate buffer at pH 5.5 for two hours at 20°C before embedding in Quetol epoxy resin and sectioning. Images were taken on an FEI Tecnai G2 transmission electron microscope operated at 120 kV using an AMT XR60B digital camera running Deben software.

Transmission electron microscopy was performed on organoids as previously described(*54*). Briefly, organoids grown in Matrigel domes were fixed directly in 24-well culture plates overnight at 4°C using 2% glutaraldehyde/2% paraformaldehyde in 1 x PBS. Following fixation, domes of Matrigel containing organoids were lifted from the plate and post-fixed in 1% osmium containing 1.5% potassium ferrocyanide before embedding in resin and sectioning. Sections were imaged using a FEI BioTwinG2 transmission electron microscope. At least 20 individual cells were imaged for each genotype.

Quantification of mitochondrial volume fraction
To determine the mitochondria volume fraction of MEFs, human cancer cell lines and organoids, at least 20 randomly obtained images per sample were taken at a direct magnification of 6500X (2D cell lines) or 11000x or higher (organoids). For 2D cell lines, a 12 x 10 grid was placed over each image and for organoids, a 16 x 16 grid was placed over each image and scaled using the STEPanizer stereology tool (https://www.ncbi.nlm.nih.gov/pubmed/21375529 (*57*)). The mitochondrial fraction was determined by computing the ratio of grid intersections that fell within mitochondria to the sum of all grid intersections that fell within a cell (mitochondrial + non-mitochondrial cellular vertices).

Quantification of cristae per mitochondrion
Cristae per mitochondrion were quantified manually from a minimum of 70 mitochondria in total per condition, taken from the TEM images of 3 independent experiments obtained as described above.

Labeled glucose and glutamine metabolomics (LC/MS)
100,000 single cells of dissociated mT organoids were plated in 300 μL of Matrigel in pre-warmed 6-cm plates overlaid with 4 mL of low glucose medium containing 1 μM doxycycline and 2 μg/mL of puromycin and cultured for 72 hours. Medium was replaced with $^{13}C_6$-glucose (Cambridge Isotopes, used at 2 mM) or $^{13}C_{5,}$ $^{15}N_2$-glutamine media (Cambridge Isotopes, used at 2mM) containing medium and organoids were collected at two time-points: 0 minutes, 45 minutes. Organoids were collected by quickly removing medium, washing cells in 1x phosphate buffered saline (PBS) and scraping cells with Matrigel on ice into 1.2 mL of cold 30% Acetonitrile: 50% Methanol. Samples were rocked for 5 minutes at 4°C before being centrifuged at 15000 g for 10 minutes at 4°C. The supernatants were transferred to new tubes and stored at -80°C before being used for LC/MS analysis. Resulting pellets were lysed in 500 μL of RIPA buffer and protein concentration was measured using the DC Protein Assay (BioRad). Domes of Matrigel (300 μl)-only were plated in 6-cm plates in triplicate, overlaid with medium and collected at the three time-points as a control.

For 2D cells, LC-MS sample preparation was performed broadly as described previously (*58, 59*). Briefly, cells were incubated in assay medium containing low glucose DMEM supplemented with 2mM uniformly labeled $^{13}C_6$-glucose, 1-$^{13}C_1$-glucose, or $^{13}C_{5,}$ $^{15}N_2$-glutamine (all from Sigma) in lieu of the unlabeled glucose or glutamine (for $^{13}C_{5,}$ $^{15}N_2$-glutamine experiments) for 45 minutes ($^{13}C_6$-glucose, $^{3}C_{5,}$ $^{15}N_2$-glutamine) or 3 hours (1-$^{13}C_1$-glucose). Metabolites were extracted by rapidly removing cell medium, washing wells once with ice-cold PBS, and lysing cells in ice-cold methanol/acetonitrile/H_2O (50:30:20) at volumes scaled based on cell counts of the counting plate to $2*10^6$ cells per mL extraction buffer. Sample plates were shaken at 4°C for 10 minutes before the extraction buffer was collected from each well, spun for 15 minutes at 16,000 g in a chilled (4°C) centrifuge, and then analyzed by LC-MS. For analysis of NADPH of 2D cells, cells were incubated in fresh medium containing or lacking 20 mM menadione for 3 hours prior to metabolite extraction.

For all LC/MS samples, metabolite analysis was performed as described previously(*60*). Briefly, a Q-exactive Orbitrap mass spectrometer (Thermo Scientific, Waltham, MA, USA) was used together with a Thermo Ultimate 3000 HPLC system to analyze prepared samples. The HPLC setup consisted of a ZIC-pHILIC column (SeQuant, 150 x 2.1 mm, 5 µm, Merck KGaA, Darmstadt, Germany), with a ZIC-pHILIC guard column (SeQuant, 20 x 2.1 mm) and an initial mobile phase of 20% 20 mM ammonium carbonate, pH 9.4, and 80% acetonitrile. Cell and medium extracts (5 µl) were injected and metabolites were separated over a 15-minute mobile phase gradient, decreasing the acetonitrile content to 20%, at a flow rate of 200 µL/min and a column temperature of 45°C. The total analysis time was 23 minutes. All metabolites were detected across a mass range of 75-1000 m/z using the Q-Exactive mass spectrometer at a resolution of 35,000 (at 200 m/z), with electrospray (ESI) ionization and polarity switching to enable both positive and negative ions to be determined in the same run. Lock masses were used, and the mass accuracy obtained for all metabolites was below 5 ppm. Data were acquired with Thermo Xcalibur software. The peak areas of different metabolites were determined using Thermo TraceFinder 4.0 software where metabolites were identified by the exact mass of the singly charged ion and by known retention time on the HPLC column. Commercial standards of all metabolites detected had been analyzed previously on this LC-MS system with the pHILIC column.

Steady-state metabolomics (GC/MS)
For GC-MS analysis of steady-state TCA cycle pools, cells were cultured in low glucose medium for 48 hours. Cells were then washed with ice-cold PBS, detached with a cell scraper

on ice, and pelleted by centrifugation. Metabolites were extracted using methanol-chloroform (2:1) and metabolic profiling was performed as previously described (*61, 62*). Briefly, the aqueous metabolites were derivatized in a solution of 20 mg/ml Methoxyamine hydrochloride in pyridine for 17 hours and then silylated with N-methyl-N-trimethylsilyltrifluoro- acetamide (MSTFA, Sigma) for one hour as previously described (*63*). The derivatized samples were diluted in hexane before being injected into a Thermo Scientific Trace Ultra Gas Chromatograph (Thermo Scientific; injector temperature: 220°C, helium carrier gas flow rate: 1.2 mL/min). The column effluent was introduced into a Trace DSQ quadrupole mass spectrometer (Thermo Scientific; transfer line temperature: 250°C, ion source temperature: 220°C, electron beam: 70 eV). The detector was turned on after a solvent delay of 120 s, and data were collected in full scan mode using 3 scans/s across a mass range of 50–650 m/z. GC-MS chromatograms were analyzed using Thermo Xcalibur software (Thermo Scientific). Metabolites were identified using the National Institute of Standards and Technology (NIST) database of mass spectra. Peaks were integrated individually in Xcalibur and then peak intensity data were further analyzed using Microsoft Excel.

Flow cytometry

Organoids were dissociated into single cells and resuspended in phenol red-free +++ medium. Adherent 2D cells were labeled for 30 minutes in serum-free and phenol-red-free DMEM. The following dyes were used: Mitotracker Green (40 nM), MitoSox Red (5 μM), $DiIC_1(5)$ (25 nM), or DCF-DA (10μM) (Life Technologies). Cells were incubated with dyes in a 37- degree, 5% CO2 incubator for 30 min before washing with 1x PBS and resuspension in phenol red-free +++ medium (dissociated organoids) or 1x PBS+ 2%FBS (2D cells). 4′,6-Diamidino-2-phenylindole dihydrochloride (DAPI, Sigma Aldrich) was added to a final concentration of 1 μg/mL to each sample and was used to identify viable cells for analysis. Stained cells were analyzed on a BD LSR-II or BD Fortessa flow cytometer using unstained cells and single color-stained cells as controls. At least 10,000 events were collected for each sample and results were analyzed using FlowJo Software. Unless otherwise stated, median fluorescence intensity values relative to control cells are reported for each probe.

mitoQC reporter assay

Suit2 and FA-6 cells were retrovirally infected with pBabe.mCherry-GFP-$FIS1_{101-152}$ (mitoQC, obtained from Dr. Stephen Tait laboratory) and selected with hygromycin (500μg/mL) (*21*). Single cell suspensions of stably infected human cancer cells treated with siRNA (NT, NIX, or p62) were analyzed by flow cytometry on a BD Fortessa based on the protocol developed for the tandem LC3-GFP-mCherry autophagy reporter (*22*) .The median derived mCherry/GFP ratio parameter was compared between samples.

Quantitative RT-PCR

RNA was isolated from cultured cells and organoids using Trizol followed by Pure Link RNA isolation kit with DNase treatment according to manufacturer's instructions. Reverse transcription was performed on 1 μg of total RNA using TaqMan Multiscribe Reverse Transcription reagents (Applied Biosystems). Quantitative real time PCR was performed on a QuantStudio 6-flex Instrument (Applied Biosystems) using Taqman probes (listed below). Relative gene expression was calculated using the ΔΔCt method with *Hprt* used as an internal control.

Hs00364284_g1 Human KRAS
Hs01087963_m1 Human NIX / BNIP3L

Hs02800695_m1 Human HPRT
Mm00786306_s1 Mouse Bnip3l
Mm00448091_m1 Mouse p62/Sqstm1
Mm00446968_m1 Mouse Hprt
Mm01135606_m1 Mouse Nrf1
Mm00489774_m1 Mouse Acsm3
Mm01208835_m1 Mouse PGC-1alpha
Mm00450187_m1 Mouse Park2
Mm00550827_m1 Mouse Pink1
Mm00448091_m1 Mouse p62/Sqstm1
Mm00517492_m1 Mouse Kras
Mm00447485_m1 Mouse Tfam

mtDNA / nDNA determination

Total DNA was extracted from cells using a DNeasy Blood and Tissue kit (Qiagen) according to the manufacturer's recommendations with modifications as previously described (*17*). For DNA extraction from pancreas and liver tissue, the Qiagen user-developed protocol 'Purification of total DNA from soft tissues using the TissueLyser and the DNeasy Blood & Tissue Kit (DY11 Aug-06)' was used. Total DNA was then quantified, diluted to 3 ng/ul, and used to determine the relative copy number of mitochondrial DNA (COX2) and nuclear DNA (Amyloid precursor protein (APP)) by quantitative PCR using a 7900HT real-time PCR machine (Life Technologies) and the primer/probe combinations listed below:

Mouse APP forward: CGGAAACGACGCTCTCATG

Mouse APP reverse: CCAGGCTGAATTCCCCAT

Mouse APP probe: TCGCTGACGGAAACCAAGACCC (FAM and TAMRA)

Mouse Cox2 forward: GAGCAGTCCCCTCCCTAGGA

Mouse Cox2 reverse: GGTTTGATGTTACTGTTGCTTGATTT

Mouse Cox2 probe: AAACTGATGCCATCCCAGGCCGA (FAM and TAMRA)

Human APP forward: TTTTTGTGTGCTCTCCCAGGTCT

Human APP reverse: TGGTCACTGGTTGGTTGGC

Human APP probe: CCCTGAACTGCAGATCACCAATGTGGTAG (FAM and TAMRA)

Human COX2 forward: CGTCTGAACTATCCTGCCCG

Human COX2 reverse: TGGTAAGGGAGGGATCGTTG

Human COX2 probe: CGCCCTCCCATCCCTACGCATC (FAM and TAMRA)

NADPH/NADP+ measurement

For mT8 organoids and 2D cell lines, the NADPH/NADP+ ratio was determined from the NADPH and NADP+ pools measured by LC-MS during metabolomic analysis. For mT5 organoids, the NADPH/NADP+ ratio was measured by first isolating organoids from Matrigel using Cell Recovery Solution (Corning) and washing with ice cold 1xPBS. Pelleted organoids were evaluated using the NADP/NADPH Assay Kit (Abcam ab65349) according to manufacturer's instructions.

Mitochondrial enrichment

The isolation of mitochondrial-enriched fractions from mouse tissue and cells was performed as previously described (*64, 65*) with modifications as detailed below. For pancreas tissue, sections (approximately 60 mg) were collected in ice-cold PBS and finely diced. Cells were incubated in 1 mg/ml collagenase V (Sigma) at 37°C for 30 minutes with mixing, pelleted by centrifugation (200 g), re-suspended in 0.25% Trypsin/EDTA (Life Technologies). Cells were then incubated at 37°C for 10 minutes with mixing followed by washing with DMEM +10%FBS. Cells were pelleted by centrifugation, washed in ice-cold PBS, and re-suspended in ice-cold isotonic HIM buffer (200 mM mannitol, 70 mM sucrose, 1 mM EGTA, 10 mM HEPES, pH 7.5) containing phosphatase inhibitors and protease inhibitors (Roche). Cultured cells were detached from cell culture dishes using 0.25% Trypsin/EDTA (Life Technologies) and pelleted. Pelleted single cells were then homogenized in an Isobiotec cell homogenizer using a steel bead to allow 18 μm of clearance through the homogenizer aperture (Isobiotec). Unbroken cells and nuclei were removed as pellets by consecutive centrifugation (at 350 g and 800 g) 4°C. The supernatant was centrifuged at 9000 g for 10 minutes at 4°C to obtain cytoplasmic (supernatant) and mitochondrial-enriched (pellet) fractions. The mitochondrial pellet was washed before lysis in RIPA buffer containing phosphatase inhibitors and protease inhibitors (Roche) and the cytoplasmic fraction was clarified by centrifugation. Both fractions were sonicated for 3 minutes at 4°C to shear any contaminating genomic DNA.

Western Blotting

Standard procedures were followed for Western blot. MEFs and human PDAC cells were prepared and analyzed as described previously (*60*) using Li-Cor secondary reagents and a Li-Cor Odyssey Infrared Scanner. Organoids and FPC cells were collected and lysed in 0.1% Triton X-100, 15 mM NaCl, 0.5 mM EDTA, 5 mM Tris, pH 7.5 with the addition of Mini-Complete protease inhibitors (Roche) and a PhosSTOP phosphatase inhibitor cocktail (Roche). Protein lysates were clarified and separated using 4-12% Bis-Tris NuPAGE gels (Life Technologies) and then transferred onto PVDF membranes (Millipore). Membranes were blocked with 5% Non-fat dry milk or 5% BSA in TBST (0.1% Tween20 in Tris-Buffered Saline), and incubated with primary antibodies overnight rocking at 4°C. Membranes were incubated with HRP-conjugated secondary antibodies for 1 hour at room temperature and detected by ECL (GE Healthcare). Primary antibodies used: CoxIV, Nix, p62, Vinculin, LC3-B, HIF-1a, Bnip3 (rodent specific) and Bnip3 (for human samples), HSP60, p62, HSP90 (used for human PDAC and MEF western blots), phospho and total p44/p42 (all from Cell Signaling Technology); CV-5/ATP5A (abcam); Hsp90 (Millipore) (for organoid and tissue extract western blots). IRDye 800CW and 680LT raised in Donkey (anti-Rabbit and anti-Mouse) secondary antibodies were used for MEF and Human PDAC western blots (LiCor) and HRP-conjugated secondary antibodies were used for protein detection in organoids and mouse cancer cell western blots (Jackson Immunoresearch).

Human Patient Survival Analysis

We obtained TCGA expression data by accessing the publicly available harmonized cancer datasets hosted on the National Cancer Institute GDC data portal (available at: https://portal.gdc.cancer.gov/). Patients whose tumors were determined to be non-PDAC by histopathological analysis were excluded (*2*). Patients were divided into high (upper 50^{th} percentile) and low (lower 50^{th} percentile) *BNIP3L* expression and Kaplan-Meier survival analysis was performed.

Data plotting and statistical analysis

All data were plotted using Prism 7 (Graph Pad). Statistical analysis for each experiment was performed using the tools within Prism 7, the indicated tests, and multiplicity-adjusted p-values. Figures were prepared using Illustrator (Adobe). All data represented as means and standard error (error bars) unless otherwise indicated. Asterisks denote p-value as follows: *p<.05, **p<.01, ***p<.001, ****p<.0001.

References

1. National Cancer Institute, *SEER Cancer Stat Facts: Pancreatic Cancer* (2017).
2. P. Bailey *et al.*, Genomic analyses identify molecular subtypes of pancreatic cancer. *Nature* **531**, 47-52 (2016).
3. J. Son *et al.*, Glutamine supports pancreatic cancer growth through a KRAS-regulated metabolic pathway. *Nature* **496**, 101-105 (2013).
4. H. Ying *et al.*, Oncogenic Kras maintains pancreatic tumors through regulation of anabolic glucose metabolism. *Cell* **149**, 656-670 (2012).
5. F. Weinberg *et al.*, Mitochondrial metabolism and ROS generation are essential for Kras-mediated tumorigenicity. *Proc Natl Acad Sci U S A* **107**, 8788-8793 (2010).
6. C. Commisso *et al.*, Macropinocytosis of protein is an amino acid supply route in Ras-transformed cells. *Nature* **497**, 633 (2013).
7. J. Y. Guo *et al.*, Activated Ras requires autophagy to maintain oxidative metabolism and tumorigenesis. *Genes Dev* **25**, 460-470 (2011).
8. J. Y. Guo *et al.*, Autophagy suppresses progression of K-ras-induced lung tumors to oncocytomas and maintains lipid homeostasis. *Genes Dev* **27**, 1447-1461 (2013).
9. R. M. Perera *et al.*, Transcriptional control of autophagy-lysosome function drives pancreatic cancer metabolism. *Nature* **524**, 361-365 (2015).
10. S. Yang *et al.*, Pancreatic cancers require autophagy for tumor growth. *Genes Dev* **25**, 717-729 (2011).
11. A. Viale *et al.*, Oncogene ablation-resistant pancreatic cancer cells depend on mitochondrial function. *Nature* **514**, 628-632 (2014).
12. G. M. DeNicola *et al.*, Oncogene-induced Nrf2 transcription promotes ROS detoxification and tumorigenesis. *Nature* **475**, 106-109 (2011).
13. S. R. Hingorani *et al.*, Preinvasive and invasive ductal pancreatic cancer and its early detection in the mouse. *Cancer Cell* **4**, 437-450 (2003).
14. S. F. Boj *et al.*, Organoid models of human and mouse ductal pancreatic cancer. *Cell* **160**, 324-338 (2015).
15. J. Yun *et al.*, Glucose deprivation contributes to the development of KRAS pathway mutations in tumor cells. *Science* **325**, 1555-1559 (2009).
16. M. R. Sullivan *et al.*, Quantification of microenvironmental metabolites in murine cancer models reveals determinants of tumor nutrient availability. *bioRxiv*, 492652 (2018).
17. S. Ayala-Torres, Y. Chen, T. Svoboda, J. Rosenblatt, B. Van Houten, Analysis of gene-specific DNA damage and repair using quantitative polymerase chain reaction. *Methods* **22**, 135-147 (2000).
18. L. E. Drake, M. Z. Springer, L. P. Poole, C. J. Kim, K. F. Macleod, Expanding perspectives on the significance of mitophagy in cancer. *Semin Cancer Biol* **47**, 110-124 (2017).
19. R. L. Schweers *et al.*, NIX is required for programmed mitochondrial clearance during reticulocyte maturation. *Proceedings of the National Academy of Sciences of the United States of America* **104**, 19500-19505 (2007).
20. H. Sandoval *et al.*, Essential role for Nix in autophagic maturation of erythroid cells. *Nature* **454**, 232-235 (2008).

21. G. F. G. Allen, R. Toth, J. James, I. G. Ganley, Loss of iron triggers PINK1/Parkin-independent mitophagy. *EMBO reports* **14**, 1127 (2013).
22. J. M. Gump, A. Thorburn, Sorting cells for basal and induced autophagic flux by quantitative ratiometric flow cytometry. *Autophagy* **10**, 1327-1334 (2014).
23. J.-H. Um, Y. Y. Kim, T. Finkel, J. Yun, Sensitive Measurement of Mitophagy by Flow Cytometry Using the pH-dependent Fluorescent Reporter mt-Keima. *JoVE*, e58099 (2018).
24. F. Sun, C. Dai, J. Xie, X. Hu, Biochemical issues in estimation of cytosolic free NAD/NADH ratio. *PloS one* **7**, e34525-e34525 (2012).
25. J. Todoric *et al.*, Stress-Activated NRF2-MDM2 Cascade Controls Neoplastic Progression in Pancreas. *Cancer Cell* **32**, 824-839 e828 (2017).
26. Y. Ichimura *et al.*, Phosphorylation of p62 Activates the Keap1-Nrf2 Pathway during Selective Autophagy. *Molecular Cell* **51**, 618-631 (2013).
27. M. Macchi *et al.*, The Drosophila inner-membrane protein PMI controls crista biogenesis and mitochondrial diameter. *Journal of Cell Science* **126**, 814 (2013).
28. R. Quintana-Cabrera *et al.*, The cristae modulator Optic atrophy 1 requires mitochondrial ATP synthase oligomers to safeguard mitochondrial function. *Nature Communications* **9**, 3399 (2018).
29. E. L. Robb *et al.*, Selective superoxide generation within mitochondria by the targeted redox cycler MitoParaquat. *Free Radical Biology and Medicine* **89**, 883-894 (2015).
30. R. Rossignol *et al.*, Energy Substrate Modulates Mitochondrial Structure and Oxidative Capacity in Cancer Cells. *Cancer Research* **64**, 985 (2004).
31. G. Sriram *et al.*, Global metabolic effects of glycerol kinase overexpression in rat hepatoma cells. *Molecular genetics and metabolism* **93**, 145-159 (2008).
32. P. Dey *et al.*, Genomic deletion of malic enzyme 2 confers collateral lethality in pancreatic cancer. *Nature* **542**, 119-123 (2017).
33. L. Jiang *et al.*, Reductive carboxylation supports redox homeostasis during anchorage-independent growth. *Nature* **532**, 255-258 (2016).
34. A. R. Mullen *et al.*, Reductive carboxylation supports growth in tumour cells with defective mitochondria. *Nature* **481**, 385-388 (2011).
35. D. R. Wise *et al.*, Hypoxia promotes isocitrate dehydrogenase-dependent carboxylation of α-ketoglutarate to citrate to support cell growth and viability. *Proceedings of the National Academy of Sciences* **108**, 19611 (2011).
36. C. M. Metallo *et al.*, Reductive glutamine metabolism by IDH1 mediates lipogenesis under hypoxia. *Nature* **481**, 380-384 (2011).
37. A. Diwan *et al.*, Unrestrained erythroblast development in Nix-/- mice reveals a mechanism for apoptotic modulation of erythropoiesis. *Proc Natl Acad Sci U S A* **104**, 6794-6799 (2007).
38. R. Lock *et al.*, Autophagy facilitates glycolysis during Ras-mediated oncogenic transformation. *Mol Biol Cell* **22**, 165-178 (2011).
39. L. Esteban-Martinez *et al.*, Programmed mitophagy is essential for the glycolytic switch during cell differentiation. *EMBO J* **36**, 1688-1706 (2017).
40. C. Li *et al.*, PINK1 and PARK2 Suppress Pancreatic Tumorigenesis through Control of Mitochondrial Iron-Mediated Immunometabolism. *Dev Cell* **46**, 441-455 e448 (2018).
41. A. H. Chourasia *et al.*, Mitophagy defects arising from BNip3 loss promote mammary tumor progression to metastasis. *EMBO reports* **16**, 1145-1163 (2015).
42. J. Lai, J. Flanagan, W. A. Phillips, G. Chenevix-Trench, J. Arnold, Analysis of the candidate 8p21 tumour suppressor, BNIP3L, in breast and ovarian cancer. *Br J Cancer* **88**, 270-276 (2003).
43. P. Fei *et al.*, Bnip3L is induced by p53 under hypoxia, and its knockdown promotes tumor growth. *Cancer Cell* **6**, 597-609.

44. H. M. Sowter, P. J. Ratcliffe, P. Watson, A. H. Greenberg, A. L. Harris, HIF-1-dependent regulation of hypoxic induction of the cell death factors BNIP3 and NIX in human tumors. *Cancer Res* **61**, 6669-6673 (2001).
45. W.-X. Zong, J. D. Rabinowitz, E. White, Mitochondria and Cancer. *Molecular cell* **61**, 667-676.
46. T. L. Yuan *et al.*, Differential Effector Engagement by Oncogenic KRAS. *Cell Rep* **22**, 1889-1902 (2018).
47. D. Burk, A. L. Schade, On respiratory impairment in cancer cells. *Science* **124**, 270-272 (1956).
48. S. Weinhouse, On respiratory impairment in cancer cells. *Science* **124**, 267-269 (1956).
49. O. Warburg, On respiratory impairment in cancer cells. *Science* **124**, 269-270 (1956).
50. S. Hui *et al.*, Glucose feeds the TCA cycle via circulating lactate. *Nature* **551**, 115-118 (2017).
51. J. Y. Guo *et al.*, Autophagy provides metabolic substrates to maintain energy charge and nucleotide pools in Ras-driven lung cancer cells. *Genes & Development* **30**, 1704-1717 (2016).
52. D. M. Tompers, P. A. Labosky, Electroporation of murine embryonic stem cells: a step-by-step guide. *Stem Cells* **22**, 243-249 (2004).
53. S. R. Hingorani *et al.*, Trp53R172H and KrasG12D cooperate to promote chromosomal instability and widely metastatic pancreatic ductal adenocarcinoma in mice. *Cancer Cell* **7**, 469-483 (2005).
54. D. Ohlund *et al.*, Distinct populations of inflammatory fibroblasts and myofibroblasts in pancreatic cancer. *J Exp Med* **214**, 579-596 (2017).
55. C. Fellmann *et al.*, An optimized microRNA backbone for effective single-copy RNAi. *Cell Rep* **5**, 1704-1713 (2013).
56. M. Tajan *et al.*, A Role for p53 in the Adaptation to Glutamine Starvation through the Expression of SLC1A3. *Cell Metabolism* **28**, 721-736.e726 (2018).
57. S. A. Tschanz, P. H. Burri, E. R. Weibel, A simple tool for stereological assessment of digital images: the STEPanizer. *J Microsc* **243**, 47-59 (2011).
58. C. F. Labuschagne, N. J. van den Broek, G. M. Mackay, K. H. Vousden, O. D. Maddocks, Serine, but not glycine, supports one-carbon metabolism and proliferation of cancer cells. *Cell Rep* **7**, 1248-1258 (2014).
59. G. M. Mackay, L. Zheng, N. J. van den Broek, E. Gottlieb, Analysis of Cell Metabolism Using LC-MS and Isotope Tracers. *Methods Enzymol* **561**, 171-196 (2015).
60. T. J. Humpton, A. K. Hock, O. D. K. Maddocks, K. H. Vousden, p53-mediated adaptation to serine starvation is retained by a common tumour-derived mutant. *Cancer & metabolism* **6**, 18-18 (2018).
61. H. J. Atherton *et al.*, A combined 1H-NMR spectroscopy- and mass spectrometry-based metabolomic study of the PPAR-alpha null mutant mouse defines profound systemic changes in metabolism linked to the metabolic syndrome. *Physiol Genomics* **27**, 178-186 (2006).
62. L. Belle *et al.*, [Validation of a diagnostic algorithm in non severe pulmonary embolism at the Annecy general hospital. D-dimers, venous lower limb ultra-sound and spiral CT scan]. *Ann Cardiol Angeiol (Paris)* **51**, 243-247 (2002).
63. J. Gullberg, P. Jonsson, A. Nordstrom, M. Sjostrom, T. Moritz, Design of experiments: an efficient strategy to identify factors influencing extraction and derivatization of Arabidopsis thaliana samples in metabolomic studies with gas chromatography/mass spectrometry. *Anal Biochem* **331**, 283-295 (2004).
64. M. Grinberg *et al.*, Mitochondrial carrier homolog 2 is a target of tBID in cells signaled to die by tumor necrosis factor alpha. *Mol Cell Biol* **25**, 4579-4590 (2005).

65. C. Frezza, S. Cipolat, L. Scorrano, Organelle isolation: functional mitochondria from mouse liver, muscle and cultured fibroblasts. *Nat Protoc* **2**, 287-295 (2007).

Figure Legends

Figure 1. Endogenous oncogenic Kras suppresses mitochondrial content

A. Median fluorescence intensity (MFI) of LSL-Kras^{G12D} MEFs infected with Adeno-Empty (WT) or Adeno-Cre (G12D) and stained with DCF-DA (cyto ROS), MitoSox Red (Mito ROS), Mitotracker Green (Mito mass), DiIC$_1$5 (Membrane potential), n=3 independent experiments. Two-way ANOVA with Holm-Sidak test.

B. Median fluorescence intensity of LSL-Kras^{G12D} organoids infected with Adeno-Empty (WT) or Adeno-Cre (G12D) and stained with Mitotracker Green (Mito mass) or DiIC$_1$5 (Membrane potential), n=3 independent experiments. One-way ANOVA with Holm-Sidak test.

C. Representative TEM micrographs of LSL-Kras^{G12D} MEFs infected with Adeno-Empty (WT) or Adeno-Cre (G12D) and grown in low-glucose media for 4 days. Scale bar: 500 nm. Black arrow: mitochondria.

D. Quantification of mitochondrial volume fraction per cell in TEM micrographs from C; n≥20 images analyzed per cell line, n=3 independent experiments. Two-tailed t-test with unequal variance.

E. Median fluorescence intensity (normalized to vehicle) of FPC 2D cell lines stained with MitoTracker Green 96 hours after treatment with vehicle or 4-OH-Tamoxifen (TAM) in low glucose medium, n=3 biological replicates. Two-tailed t-test with unequal variance.

F. Median fluorescence intensity of siNT (non-targeting control) or siKRAS-treated (KR) human cell lines stained with MitoTracker Green normalized to siNT, n=3 independent experiments per cell line. One-way ANOVA with Holm-Sidak test.

Figure 2. Oncogenic Kras supports Nix expression

A. Nix and p62 protein levels in the cytoplasmic and mitochondrial-enriched fractions from LSL-Kras^{G12D} MEFs infected with Adeno-Empty (WT) or Adeno-Cre (G12D). Hsp90 is used as cytoplasmic loading control and CoxIV is used as mitochondrial loading control.

B. Nix and LC3-II protein levels in LSL-Kras^{G12D} organoids infected with Adeno-Empty (WT) or Adeno-Cre (G12D). Vinculin is used as a loading control.

C. Nix protein levels in organoids derived from normal pancreatic ducts, PanIN lesions, or PDAC (tumor).

D. Representative IHC staining for Nix or p62 on tissue sections showing normal pancreas (WT), PanIN (KC), PDAC (KPC), or lung metastases (KPC). Black arrowhead: normal duct, white arrowhead: PanIN lesion, blue arrowhead: PDAC. Scale bar=50μm.

E. Representative IHC staining for NIX in Human PanIN and PDAC tissue. Black arrows: PanIN, black arrowhead: normal duct, blue arrowhead: PDAC.

F. Nix protein levels in FPC 2D cell line treated with vehicle or 4-OH-Tamoxifen (TAM) for 96 hours in low glucose medium.

Figure 3. Nix mediates suppression of mitochondrial mass to promote proliferation in Kras-mutant cells

A. Nix protein levels in mitochondrial fraction of pancreatic protein lysates from wild-type (WT) and LSL-Kras^{G12D}; Pdx1-cre (KC) aged mice (9 months). N=7 each. CoxIV is used as loading control.

B. mtDNA/nDNA ratio for pancreata isolated from KC and WT mice in A, normalized to WT (n=5 mice per genotype). Unpaired t-test with Welch's correction.

C. Median fluorescence intensity of siNT and siNix-treated LSL-Kras^{G12D} MEFs previously infected with Adeno-Empty (WT) or Adeno-Cre (G12D) and stained with MitoSox Red (Mito ROS), Mitotracker Green (Mito mass), and DiIC$_1$5 (Membrane potential).Median fluorescent intensity (MFI) normalized to siNT, n=3 independent experiments. Two-way ANOVA with Holm-Sidak test.

D. Median fluorescence intensity of siNT and siNIX Suit2 and FA6 human cancer cells stained with MitoSox Red (Mito ROS), Mitotracker Green (Mito mass), and DiIC$_1$5 (Membrane potential). Median fluorescent intensity (MFI) normalized to siNT, n=5 independent experiments. Two-way ANOVA with Holm-Sidak test.

E. Median fluorescence intensity of non-targeting control (NT) and siMAP2K2/MEK2 FA6 cells stained with MitoSox Red (Mito ROS), Mitotracker Green (Mito mass), and DiIC$_1$5 (Membrane potential). Median fluorescent intensity (MFI) normalized to siNT, n=3 independent experiments. Two-way ANOVA with Holm-Sidak test.

F. Relative proliferation ratio (Day 4 / Day 0 counts) for siNT and siNIX FA6 and Suit2 cells grown in either full glucose medium (25 mM, n=4 independent experiments) or low glucose medium (0.5 mM, n=5 independent experiments, Two-way ANOVA with Holm-Sidak test).

Figure 4. Kras- and Nix-mediated mitophagy limits mitochondrial glucose flux and supports redox regulation

A. Oxygen consumption rate (OCR) of tumor (mT) organoids infected with LEPG-hairpins against *Nix* (shNix447) or *Renilla* luciferase (shRluc713) as a control, cultured in low glucose medium, normalized to covered area. Dotted lines (from left to right) represent injections of Oligomycin (Oli, 1 μM), FCCP (1 μM) and Rotenone/Antimycin A (Rot/Ant, 0.5 μM). Representative experiment of 2 independent experiments. n=5 technical replicates per experiment (mean±s.d.). Two-way ANOVA with Holm-Sidak test.

B. Basal and maximal OCR per cell of Suit2 and FA6 cells treated with NIX siRNA and grown in low glucose media normalized to siNT cells. n=5 independent experiments. Two-way ANOVA with Holm-Sidak test. All comparisons significant at $p<0.05$.

C. Representative TEM images of mitochondria from siNT and siNIX-treated FA6 and Suit2 cells. Scale bar: 500 nm.

D. Quantification of number of cristae per mitochondrion. $N \geq 70$ mitochondria analyzed per cell line per condition. Two-way ANOVA with Holm-Sidak test.

E. Relative mitochondrial ROS (MitoSox Red fluorescence) level normalized to mitochondrial mass (MitoTracker Green fluorescence) for siNT and siNIX FA6 and Suit2 cells as determined by flow cytometry. n=3 independent experiments. Two-way ANOVA with Holm-Sidak test.

F. Relative proliferation of siNT and siNIX human 2D cells in (glucose-free) galactose-containing (5g/L) media after 72 hours. n= 4 independent experiments. Two-way ANOVA with Holm-Sidak test.

G. Steady-state pool sizes/cell of Succinate and Malate in siNT and siNIX-treated LSL-$Kras^{G12D}$ MEFs previously infected with Adeno-Empty (WT) or Adeno-Cre (G12D) and cultured in low glucose conditions. n=5 independent experiments for WT/G12D NT, and n=3 for siNIX cells. Two-way ANOVA with Holm-Sidak test.

H. Isotopologue analysis of glycolytic and TCA cycle intermediates: glucose-6-phosphate (G6P), ribose-5-phosphate (R5P), dihydroxyacetone phosphate (DHAP), glyceraldehyde-3-phosphate (G3P), pyruvate (PYR), lactate (LAC), citrate (CIT) for siNT and siNIX FA6 cells cultured with 2mM $^{13}C_6$-glucose for 45'. n=3 independent experiments

I. Ratio of citrate (m+2) to lactate (m+3) for siNT and siNIX FA6 cells. n=3 independent experiments. Unpaired t-test with Welch's correction.

J. Ribose-5-Phosphate m+0/m+1 ratio of untreated or menadione-treated (25 μM) siNT and siNIX FA6 cells cultured with 2mM 1-$^{13}C_1$-glucose for 3 hours (n=3 replicates per condition). Two-way ANOVA with Holm-Sidak test, all $p<0.05$.

K. NADPH/NADP+ ratio relative to siNT of untreated or menadione-treated siNT and siNIX FA6 cells from J, (n=3 replicates per condition). Two-way ANOVA with Holm-Sidak test, all $p<0.05$.

L. NADPH/NADP+ ratio relative to siNT of siNT and siNIX Suit2 cells cultured in low glucose conditions (n=3 independent experiments). Unpaired t-test with Welch's correction.

M. NADPH/NADP+ ratio relative to shRluc.713 (Rluc) for RT3.shNix447 or LEPG.shNix447 (NIX) mT8 organoids cultured in low glucose conditions (n=3 replicates per condition). Unpaired t-test with Welch's correction.

Figure 5. Nix loss delays cancer progression in Kras-driven models of PDAC

A. Representative images of hematoxylin and eosin (H&E) staining of the pancreata in 9-12-month-old KC and KC $Nix^{\Delta/\Delta}$ mice, 1.5x magnification. Inset image: 20X magnification, scale bar: 200 μm). n=5 mice per genotype.

B. Quantification of the fraction of normal pancreas remaining in 9-12-month-old KC and KC $Nix^{\Delta/\Delta}$ mice. n=5 mice per genotype. Unpaired two-tailed t-test.

C. Representative images of H&E staining of the lesions found in 9-12-month-old KC and KC $Nix^{\Delta/\Delta}$ mice. n=5 mice per genotype. Scale bar: 100 μm.

D. Classification of highest grade PanIN lesions present in 9-12-month-old KC and KC $Nix^{\Delta/\Delta}$ mice. n=5 mice per genotype.

E. Representative images of H&E staining of the lesions found in 4-month-old KPC and KPC $Nix^{\Delta/\Delta}$ mice. n=5 mice per genotype. Scale bar: 100 μm.

F. Classification of highest-grade lesions present in 4-month-old KPC and KPC $Nix^{\Delta/\Delta}$ mice. n=5 mice per genotype. CPN: Cystic Papillary Neoplasm.

Figure 6: Nix suppresses mitochondrial content and promotes PDAC lethality

A. Representative immunofluorescent (IF) staining for Tom20 (green) with DAPI counterstain (blue) of PanIN lesions from 4-month-old KPC and KPC $Nix^{\Delta/\Delta}$ mice.

B. Quantification of area ($pixels^2$) of mitochondria (by Tom20 IF) normalized to number of nuclei for 4-month-old KPC and KPC $Nix^{\Delta/\Delta}$. 1 pixel=0.03 μm, n=6 images per genotype. Unpaired two-tailed t-test with equal variance.

C. Kaplan-Meier survival curve of percent survival for KPC (n=31) and KPC $Nix^{\Delta/\Delta}$ (n=32) mice. Notches represent enrolled mice that died from causes other than tumor (i.e. lymphoma, papilloma). Log-rank Mantel-Cox test.

D. Kaplan-Meier survival analysis of PDAC patients from TCGA with either elevated (above 50^{th} percentile) or low (below 50^{th} percentile) mRNA expression of BNIP3L. n= 78 patients each arm. Log-rank Mantel-Cox test.

E. Representative IF staining for Tom20 with DAPI counterstain of tumor lesions at end point in survival study of KPC and KPC $Nix^{\Delta/\Delta}$ mice.

F. Quantification of area ($pixel^2$) of mitochondria (by Tom20 IF) normalized to nuclei for survival study KPC and KPC $Nix^{\Delta/\Delta}$ mice (KPC: n=11 images, KPC $Nix^{\Delta/\Delta}$: n=14 images). Unpaired two-tailed t-test with equal variance.

G. Immunoblot showing protein levels of Nix, LC3-II, p62, Bnip3, and Hsp90 (loading control) in whole cell lysates from 3 independent lines of KPC or KPC $Nix^{\Delta/\Delta}$ tumor organoids treated with Chloroquine (CQ, 25 μM) or vehicle for 24 hours in low glucose medium.

H. Representative IHC staining for Bnip3 in KPC and KPC$Nix^{\Delta/\Delta}$ tumors, scale bar (inset): 50μm.

I. Fraction of tumor sections positive or negative for Bnip3 IHC staining, n=11 mice per genotype.

Figure 1

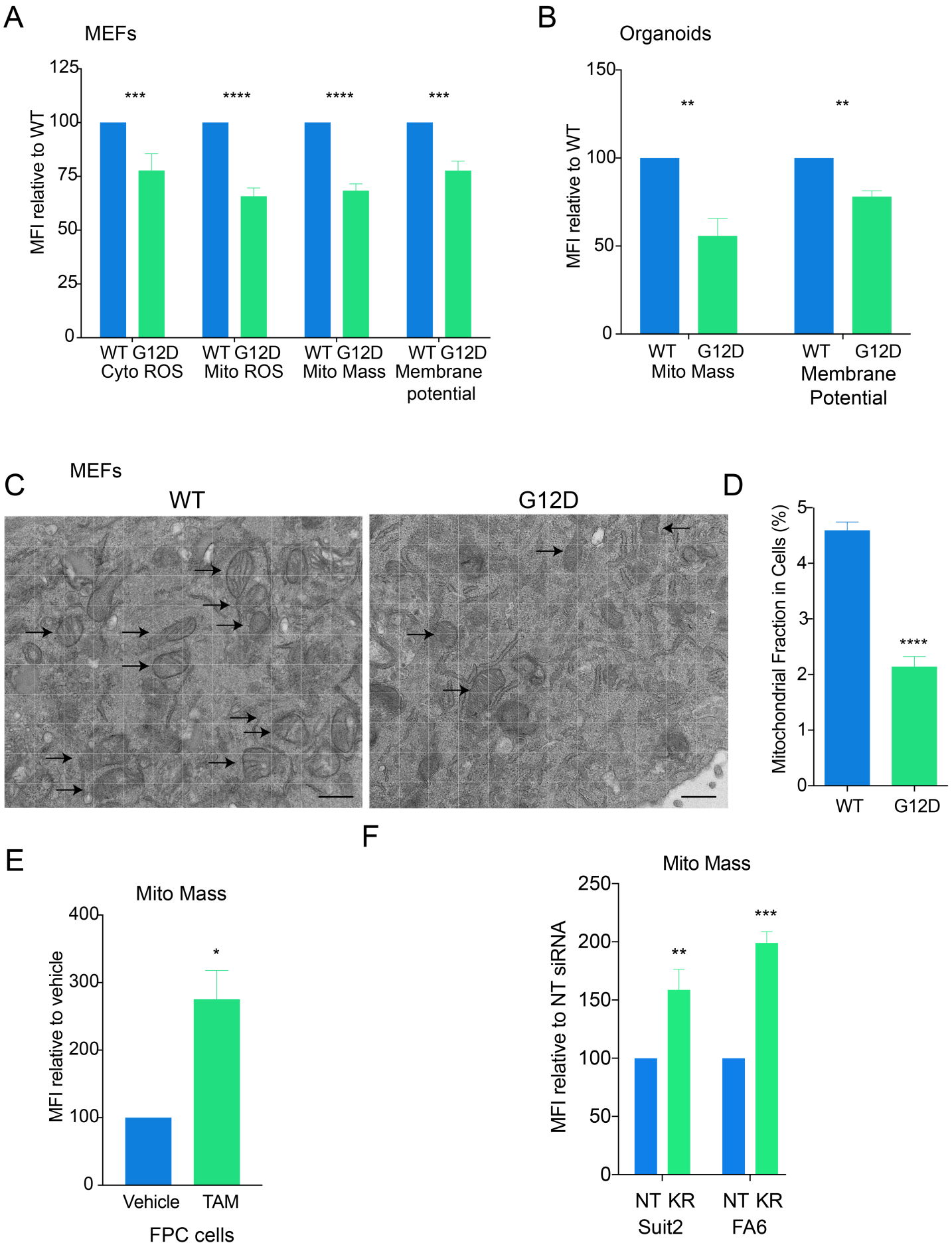
A
MEFs
MFI relative to WT
125
100
75
50
25
0
***
****
****
***
WT G12D
Cyto ROS
WT G12D
Mito ROS
WT G12D
Mito Mass
WT G12D
Membrane potential
B
Organoids
MFI relative to WT
150
100
50
0
**
**
WT G12D
Mito Mass
WT G12D
Membrane Potential
C
MEFs
WT
G12D
D
Mitochondrial Fraction in Cells (%)
5
4
3
2
1
0
****
WT
G12D
E
Mito Mass
MFI relative to vehicle
400
300
200
100
0
*
Vehicle
TAM
FPC cells
F
Mito Mass
MFI relative to NT siRNA
250
200
150
100
50
0
**
***
NT KR
Suit2
NT KR
FA6

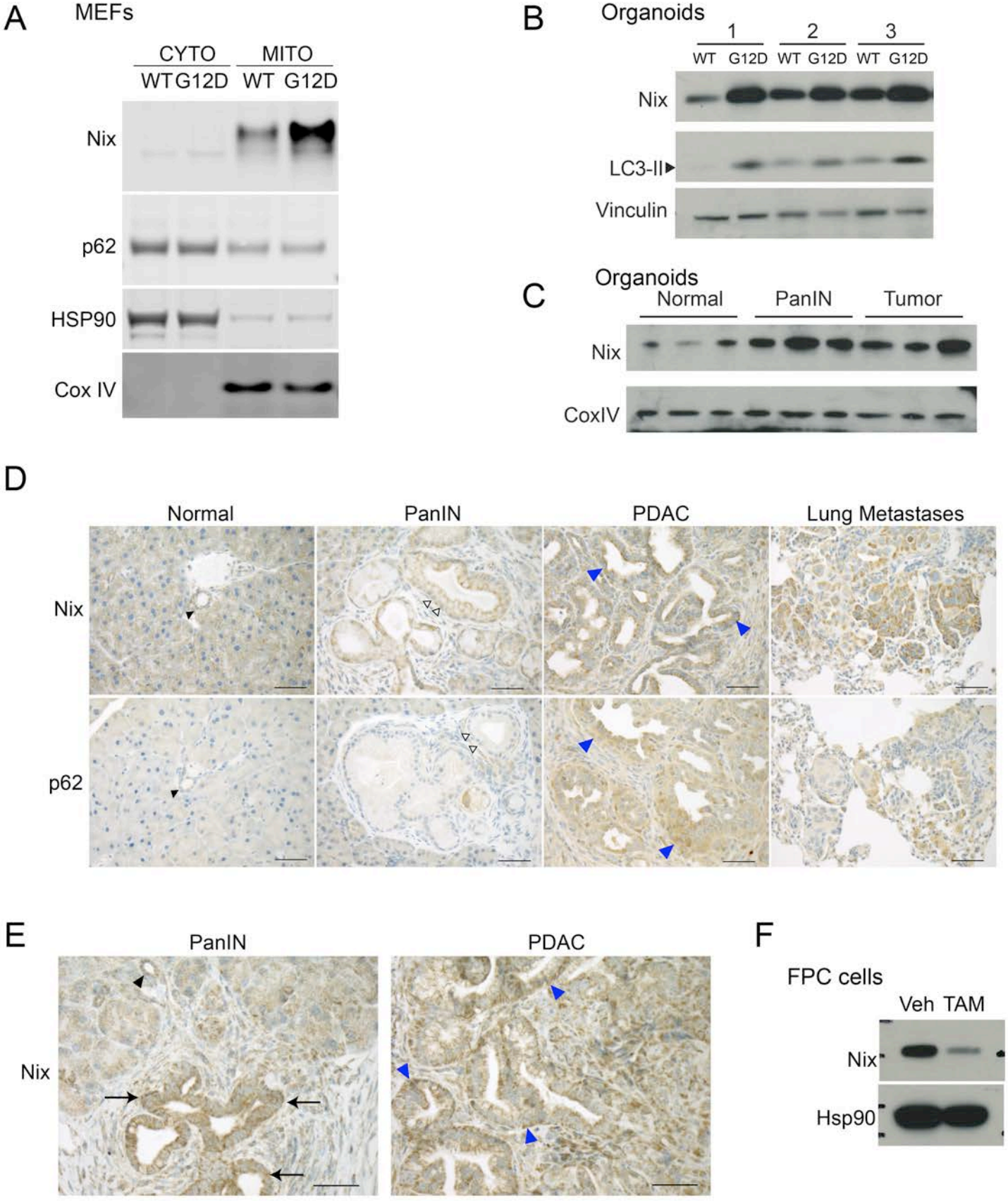
A
MEFs
CYTO
MITO
WT G12D WT G12D
Nix
p62
HSP90
Cox IV
B
Organoids
1
2
3
WT G12D WT G12D WT G12D
Nix
LC3-II
Vinculin
C
Organoids
Normal
PanIN
Tumor
Nix
CoxIV
D
Normal
PanIN
PDAC
Lung Metastases
Nix
p62
E
PanIN
PDAC
Nix
F
FPC cells
Veh TAM
Nix
Hsp90

Figure 3

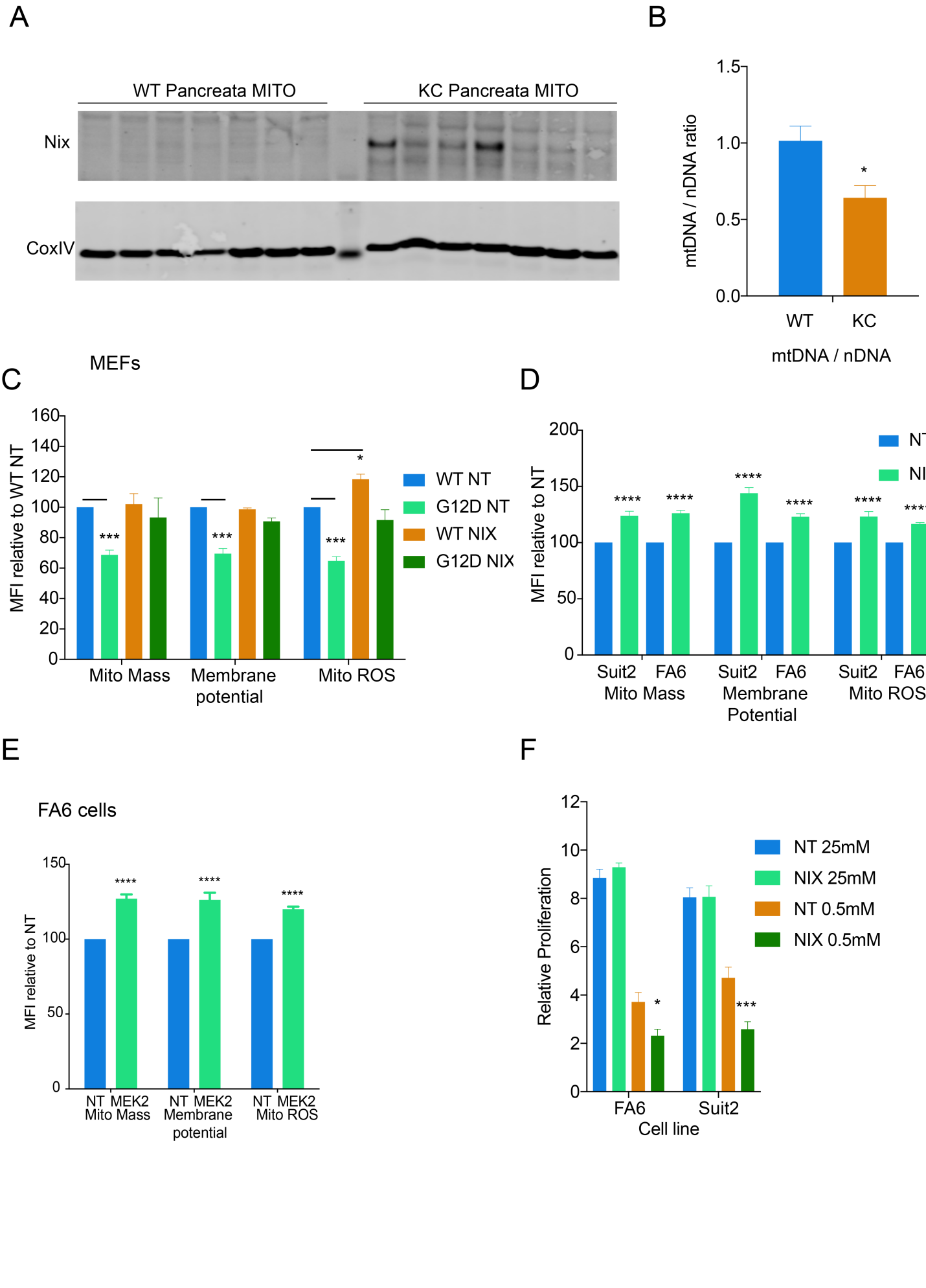
A
WT Pancreata MITO
KC Pancreata MITO
Nix
CoxIV
B
mtDNA / nDNA ratio
1.5
1.0
0.5
0.0
*
WT
KC
mtDNA / nDNA
C
MEFs
MFI relative to WT NT
160
140
120
100
80
60
40
20
0
***
***
***
*
Mito Mass
Membrane potential
Mito ROS
WT NT
G12D NT
WT NIX
G12D NIX
D
MFI relative to NT
200
150
100
50
0
****
NT
NIX
Suit2
FA6
Mito Mass
Membrane Potential
Mito ROS
E
FA6 cells
MFI relative to NT
150
100
50
0
****
NT
MEK2
Mito Mass
Membrane potential
Mito ROS
F
Relative Proliferation
12
10
8
6
4
2
0
*
***
NT 25mM
NIX 25mM
NT 0.5mM
NIX 0.5mM
FA6
Suit2
Cell line

Figure 4

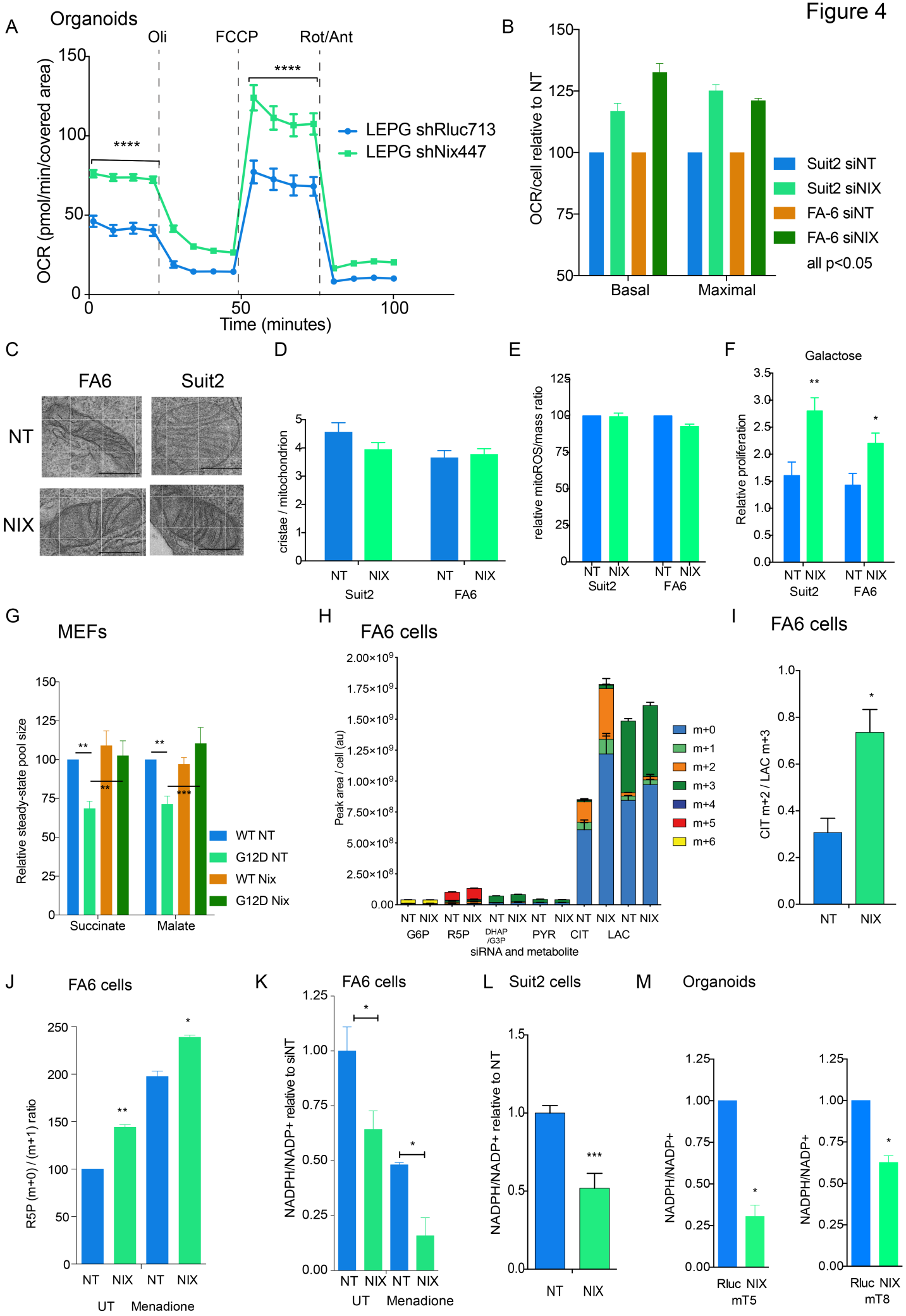
A
Organoids
Oli
FCCP
Rot/Ant
OCR (pmol/min/covered area)
Time (minutes)
LEPG shRluc713
LEPG shNix447
****
B
OCR/cell relative to NT
Basal
Maximal
Suit2 siNT
Suit2 siNIX
FA-6 siNT
FA-6 siNIX
all p<0.05
C
FA6
Suit2
NT
NIX
D
cristae / mitochondrion
Suit2
FA6
E
relative mitoROS/mass ratio
F
Galactose
Relative proliferation
G
MEFs
Relative steady-state pool size
Succinate
Malate
WT NT
G12D NT
WT Nix
G12D Nix
H
FA6 cells
Peak area / cell (au)
siRNA and metabolite
G6P
R5P
DHAP /G3P
PYR
CIT
LAC
m+0
m+1
m+2
m+3
m+4
m+5
m+6
I
FA6 cells
CIT m+2 / LAC m+3
J
FA6 cells
R5P (m+0) / (m+1) ratio
UT
Menadione
K
FA6 cells
NADPH/NADP+ relative to siNT
L
Suit2 cells
NADPH/NADP+ relative to NT
M
Organoids
NADPH/NADP+
Rluc
NIX
mT5
mT8

Figure 5

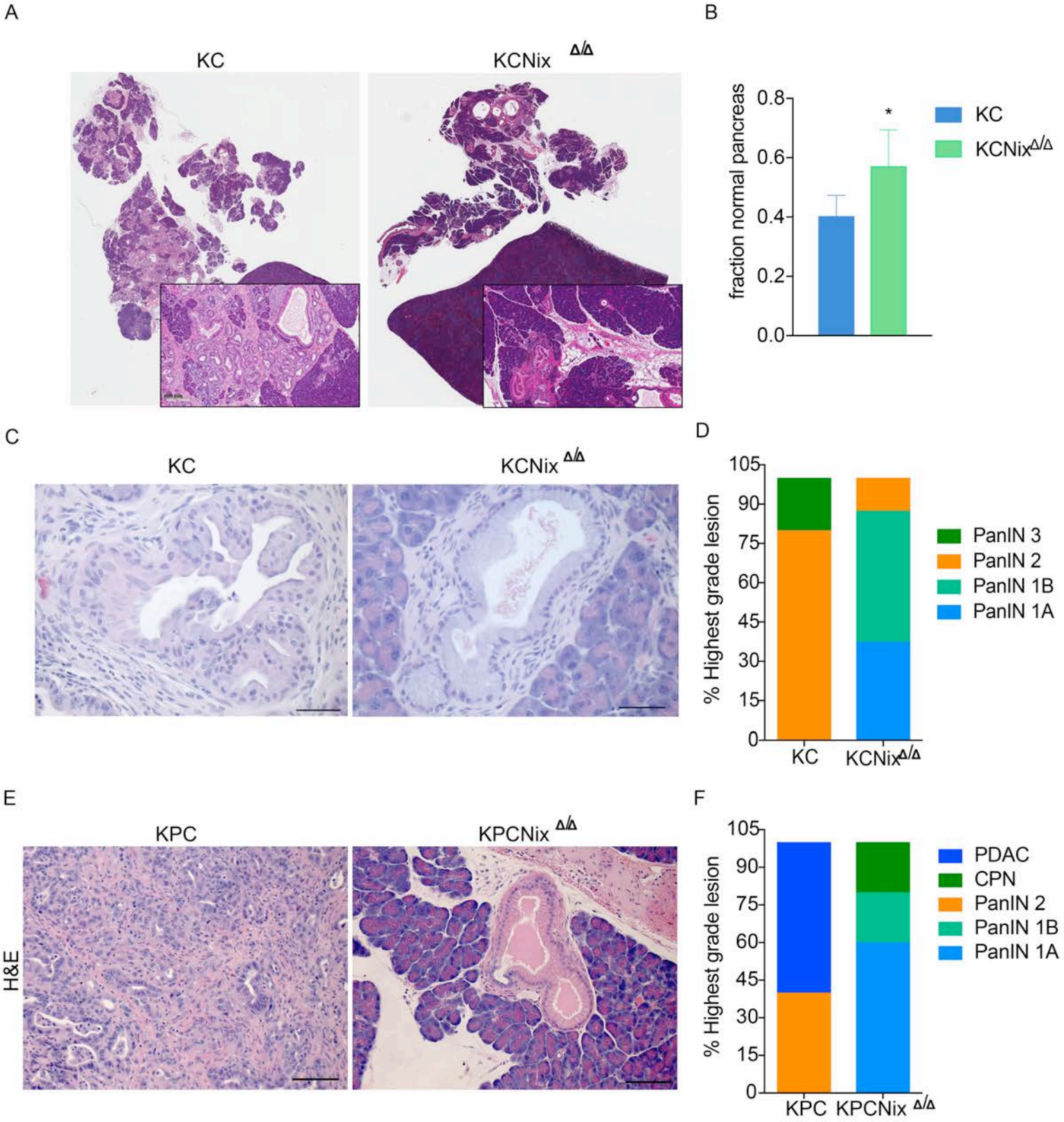
A
KC
KCNix Δ/Δ
B
fraction normal pancreas
0.8
0.6
0.4
0.2
0.0
*
KC
KCNixΔ/Δ
C
KC
KCNix Δ/Δ
D
% Highest grade lesion
105
90
75
60
45
30
15
0
KC
KCNixΔ/Δ
PanIN 3
PanIN 2
PanIN 1B
PanIN 1A
E
KPC
KPCNix Δ/Δ
H&E
F
% Highest grade lesion
105
90
75
60
45
30
15
0
KPC
KPCNix Δ/Δ
PDAC
CPN
PanIN 2
PanIN 1B
PanIN 1A

Figure 6

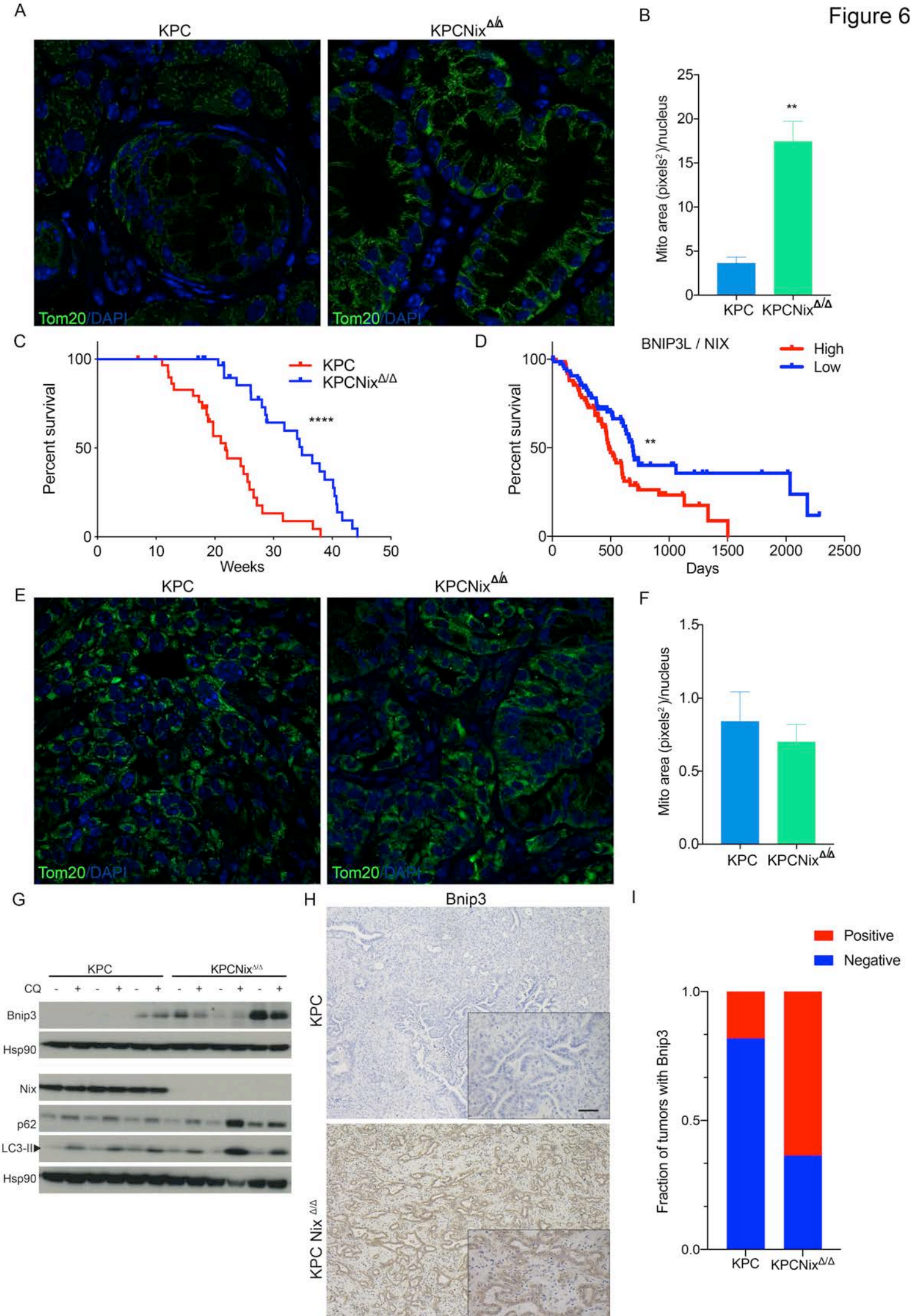
A
KPC
KPCNix$^{\Delta/\Delta}$
Tom20/DAPI
Tom20/DAPI
B
Mito area (pixels^2)/nucleus
25
20
15
10
5
0
**
KPC
KPCNix$^{\Delta/\Delta}$
C
Percent survival
100
50
0
KPC
KPCNix$^{\Delta/\Delta}$
****
0
10
20
30
40
50
Weeks
D
BNIP3L / NIX
High
Low
Percent survival
100
50
0
**
0
500
1000
1500
2000
2500
Days
E
KPC
KPCNix$^{\Delta/\Delta}$
Tom20/DAPI
Tom20/DAPI
F
Mito area (pixels^2)/nucleus
1.5
1.0
0.5
0.0
KPC
KPCNix$^{\Delta/\Delta}$
G
KPC
KPCNix$^{\Delta/\Delta}$
CQ - + - + - + - + - + - +
Bnip3
Hsp90
Nix
p62
LC3-II
Hsp90
H
Bnip3
KPC
KPC Nix$^{\Delta/\Delta}$
I
Positive
Negative
Fraction of tumors with Bnip3
1.0
0.5
0.0
KPC
KPCNix$^{\Delta/\Delta}$